Translational and HIF-1α-Dependent Metabolic Reprogramming Underpin Metabolic Plasticity and Responses to Kinase Inhibitors and Biguanides

Graphical Abstract

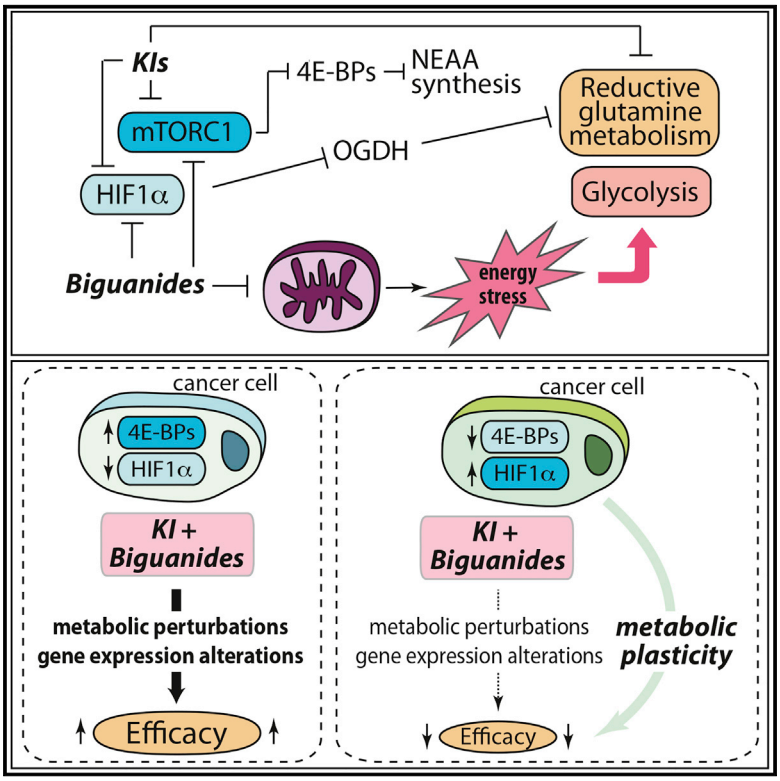

Highlights

- Kinase inhibitors (KIs) and biguanides synergistically target cancer cells
- mTORC1/4E-BP axis regulates aspartate, asparagine, and serine biosynthetic enzymes
- 4E-BPs and HIF-1α determine responses to KI/biguanide combinations
- Cancer cell metabolic plasticity limits efficacy of the KI/biguanide combinations

Authors

Laura Hulea, Simon-Pierre Gravel, Masahiro Morita, ..., Julie St-Pierre, Michael Pollak, Ivan Topisirovic

Correspondence

michael.pollak@mcgill.ca (M.P.), ivan.topisirovic@mcgill.ca (I.T.)

In Brief

Hulea et al. investigate the mechanisms underlying the synergic efficacy of kinase inhibitors (KIs) and biguanides in targeting cancer cells and show that different pathways involving mTORC1, 4E-BP, and HIF-1α are at play. Cancer cells display metabolic plasticity by engaging non-redundant adaptive mechanisms, which allows them to survive therapy combinations.

Translational and HIF-1α-Dependent Metabolic Reprogramming Underpin Metabolic Plasticity and Responses to Kinase Inhibitors and Biguanides

Laura Hulea,[1,2,19] Simon-Pierre Gravel,[3,4,5,19] Masahiro Morita,[6,7,19] Marie Cargnello,[1,2,8] Oro Uchenunu,[1,9] Young Kyuen Im,[1,9] Camille Lehuédé,[3,9] Eric H. Ma,[3,10] Matthew Leibovitch,[1,2] Shannon McLaughlan,[1,2] Marie-José Blouin,[1] Maxime Parisotto,[11] Vasilios Papavasiliou,[3] Cynthia Lavoie,[3] Ola Larsson,[12] Michael Ohh,[13] Tiago Ferreira,[14] Celia Greenwood,[1,15,16] Gaëlle Bridon,[3] Daina Avizonis,[3] Gerardo Ferbeyre,[17] Peter Siegel,[3,4] Russell G. Jones,[3,10] William Muller,[3,4,9] Josie Ursini-Siegel,[1,2,3,4,9] Julie St-Pierre,[3,4,18] Michael Pollak,[1,2,3,9,*] and Ivan Topisirovic[1,2,4,9,20,*]

[1]Lady Davis Institute, SMBD JGH, McGill University, Montreal, QC H3A 1A3, Canada
[2]Gerald Bronfman Department of Oncology, McGill University, Montreal, QC H3A 1A3, Canada
[3]Goodman Cancer Research Centre, McGill University, Montreal, QC H3A 1A3, Canada
[4]Department of Biochemistry, McGill University, Montreal, QC H3A 1A3, Canada
[5]Faculté de Pharmacie, Université de Montréal, C.P. 6128, Succursale Centre-Ville, Montréal, QC, Canada
[6]Department of Molecular Medicine and Barshop Institute for Longevity and Aging Studies, University of Texas Health Science Center at San Antonio, San Antonio, TX 78229, USA
[7]Institute of Resource Developmental and Analysis, Kumamoto University, Kumamoto 860-8111, Japan
[8]Centre de Recherche en Cancérologie de Toulouse, 31100 Toulouse, France
[9]Department of Experimental Medicine, McGill University, Montreal, QC H3A 1A3, Canada
[10]Department of Physiology, McGill University, Montreal, QC H3A 1A3, Canada
[11]Département de Chimie, Université de Montréal, Montréal, QC H3C 3J7, Canada
[12]Department of Oncology-Pathology, Science for Life Laboratory, Karolinska Institutet, 171 16 Stockholm, Sweden
[13]Department of Laboratory Medicine and Pathobiology and Department of Biochemistry, University of Toronto, Toronto, ON M5S1A8, Canada
[14]McGill University Centre for Research in Neuroscience, Montreal General Hospital, Montreal, QC H3G 1A4, Canada
[15]Department of Epidemiology, Biostatistics, and Occupational Health, McGill University, Montreal, QC H3A 1A3, Canada
[16]Department of Human Genetics, McGill University, Montreal, QC H3A 1A3, Canada
[17]Département de Biochimie et Médecine Moléculaire, Université de Montréal, Montréal, QC H3C 3J7, Canada
[18]Department of Biochemistry, Microbiology, and Immunology, Ottawa Institute of Systems Biology, University of Ottawa, Ottawa, ON K1H 8M5, Canada
[19]These authors contributed equally
[20]Lead Contact
*Correspondence: michael.pollak@mcgill.ca (M.P.), ivan.topisirovic@mcgill.ca (I.T.)
https://doi.org/10.1016/j.cmet.2018.09.001

SUMMARY

There is increasing interest in therapeutically exploiting metabolic differences between normal and cancer cells. We show that kinase inhibitors (KIs) and biguanides synergistically and selectively target a variety of cancer cells. Synthesis of non-essential amino acids (NEAAs) aspartate, asparagine, and serine, as well as glutamine metabolism, are major determinants of the efficacy of KI/biguanide combinations. The mTORC1/4E-BP axis regulates aspartate, asparagine, and serine synthesis by modulating mRNA translation, while ablation of 4E-BP1/2 substantially decreases sensitivity of breast cancer and melanoma cells to KI/biguanide combinations. Efficacy of the KI/biguanide combinations is also determined by HIF-1α-dependent perturbations in glutamine metabolism, which were observed in VHL-deficient renal cancer cells. This suggests that cancer cells display metabolic plasticity by engaging non-redundant adaptive mechanisms, which allows them to survive therapeutic insults that target cancer metabolism.

INTRODUCTION

Metabolic perturbations in cancer are required to sustain neoplastic growth (Vander Heiden and DeBerardinis, 2017). Metabolic differences between normal and cancer cells may provide a window to selectively target neoplasia (Vander Heiden and DeBerardinis, 2017). The efficacy of clinically used kinase inhibitors (KIs) is associated with alterations in key metabolic pathways, including glycolysis (Poliaková et al., 2018). Metformin (an anti-diabetic biguanide) induces energy stress via complex I inhibition and oxidative phosphorylation (OXPHOS) reduction (Andrzejewski et al., 2014; Bridges et al., 2014; Wheaton et al., 2014), which leads to a compensatory increase in glycolysis (Javeshghani et al., 2012). Biguanides exhibit anti-neoplastic effects in a variety of cancer models (DeBerardinis and Chandel, 2016). Phenformin is a more potent complex I

inhibitor than metformin (Bridges et al., 2014), and although it is associated with a higher risk of lactic acidosis than metformin, it is less toxic than many commonly used anti-cancer drugs.

Interventions that reduce glycolysis, including 2-DG (Ben Sahra et al., 2010) or glucose deprivation (Javeshghani et al., 2012), sensitize cancer cells to biguanides. As KIs also reduce glycolysis (Pollak, 2013), this provides a rationale for KI/biguanide combinations. Indeed, biguanides potentiate effects of BRAF and ERK inhibitors in melanoma (Trousil et al., 2017; Yuan et al., 2013). However, the mechanisms that underpin anti-neoplastic effects of KI/biguanide combinations are largely unknown. Herein, metabolic perturbations driven by diverse oncogenic kinases were systematically probed with KI/phenformin combinations. This revealed that metabolic plasticity, whereby cancer cells engage multiple, non-overlapping metabolic adaptations in response to therapies, may limit responses.

RESULTS

Phenformin and KIs Exhibit Synergistic Effects across Different Cancer Cell Lines

KI/biguanide combinations are effective in melanoma cells (Trousil et al., 2017; Yuan et al., 2013). To establish the generality of these findings, we used KI/phenformin combinations in cancer cells of different origin: normal murine mammary gland (NMuMG) cells transformed with oncogenic Neu/ErbB2 (V664E) (NMuMG–NT2197, hereafter referred to as NT2197; Ursini-Siegel et al., 2008), PLX4032-responsive BRAF-mutated A375 melanoma (Giard et al., 1973), imatinib-responsive BCR-ABL-positive K562 myelogenous leukemia (Lozzio and Lozzio, 1975), lapatinib-responsive VHL-deficient renal cancer RCC4 (Brodaczewska et al., 2016), and HCT116 colorectal cancer (CRC) cells (Brattain et al., 1981).

Lapatinib is a dual HER2/epidermal growth factor receptor (EGFR) inhibitor approved for treatment of HER2-amplified BCa (Geyer et al., 2006). NT2197 ErbB2-driven BCa cells were treated with increasing concentrations of lapatinib, phenformin, or combinations thereof. A concentration of phenformin (100 μM) that only marginally inhibited proliferation sensitized NT2197 cells to lapatinib (Figures 1A and S1A–S1C), whereas low concentrations of lapatinib (75 nM) increased the anti-proliferative effects of phenformin (Figures S1D and S1E). At these concentrations, the phenformin/lapatinib combination exerted only minor effects on proliferation of non-malignant cells, including parental, non-transformed NMuMG cells, mouse embryonic (MEFs), or lung fibroblasts (IMR90), which express EGFR, but in which HER2 is not amplified (Figures 1A and S1F–S1J). We next determined the combination index (CI50; Tallarida, 2006) of the lapatinib/phenformin interaction, which revealed synergistic anti-proliferative effects (CI50 ~0.8; Figures 1B and S1K). Accordingly, when combined, these drugs decreased the survival of NT2197 cells to a much greater extent than either drug alone (Figure S1L). Parallel results were observed in all the cancer cell lines tested, indicating that KIs and phenformin synergize independently of the type of the driving oncogene and cancer origin (Figures 1C–1E, S1M–S1R, and S2A–S2G).

To establish whether, as reported for melanoma (Yuan et al., 2013), these effects also occur *in vivo*, we employed NT2197 xenograft model (Ursini-Siegel et al., 2008). Consistent with cell culture observations, single drugs only modestly inhibited tumor growth (~20% of control), whereas their combination resulted in a more potent anti-neoplastic effect (~50% of control, $p = 0.0002$) (Figure 1F). Tumors were not eradicated, which is explained by the aggressive nature of the model (Ursini-Siegel et al., 2008). The anti-proliferative effects of lapatinib were potentiated by phenformin (Figures 1G, S2H, and S2I). Of note, the absolute number of apoptotic cells in tumors was lower than in cell culture, consistent with efficient removal of apoptotic cells by phagocytes *in vivo* (Poon et al., 2014) and lower achievable concentration of phenformin in plasma (~2 μM) and tissues (~1 μM) (Table S1) versus cell culture (~100–250 μM). Thus, phenformin-induced enhancement of anti-tumor efficacy of KIs *in vivo* is not confined to melanoma models.

KIs and Biguanides Have Distinct Effects on Cancer Metabolome

We next sought to identify metabolic pathways that underlie lapatinib/phenformin synergy. The lapatinib/phenformin combination, but not each drug alone, significantly reduced ATP levels in NT2197 cells (Figure S2J). As expected, phenformin increased lactate while strongly decreasing citrate and succinate levels, which reflects reduced CAC activity due to complex I inhibition and compensatory increase in glycolysis (Figure 2A) (Gravel et al., 2014; Javeshghani et al., 2012). In contrast, lapatinib reduced lactate levels, in agreement with previous observations that KIs suppress glycolysis (Pollak, 2013) and decrease ^{18}F-fludeoxyglucose (FDG) uptake in patients (McArthur et al., 2012). Lapatinib and phenformin exhibited opposite effects on the CAC intermediates fumarate, malate, citrate, and α-ketoglutarate (α-KG), suggesting that KIs may impede biguanide-induced metabolic adaptations (Figure 2A). Indeed, KIs attenuated phenformin-induced alterations of these CAC intermediates (Figure 2A) and aspartate (Figures 2A and S2K). In turn, lapatinib and phenformin increased serine, glycine, and proline, while reducing methionine levels (Figure 2A, lower panel). Glucose uptake and the lactate/pyruvate ratio were increased by phenformin and reduced by lapatinib (Figures 2B and 2C). These findings demonstrate that lapatinib opposes the phenformin-induced increase in glycolysis. Accordingly, pyruvate supplementation decreased the anti-proliferative effects of lapatinib/phenformin combination (Figure S2L).

Phenformin also increased α-KG/citrate ratio (Figure 2D), which is associated with induction of reductive glutamine metabolism that allows the synthesis of CAC intermediates for biosynthetic pathways, including lipogenesis, and is implicated in maintaining REDOX homeostasis when OXPHOS is inhibited (Gravel et al., 2014; Jiang et al., 2016; Mullen et al., 2011). Lapatinib suppressed the phenformin-induced increase in the α-KG/citrate ratio (Figure 2D). $^{13}C_5$-glutamine tracing experiments confirmed that phenformin induces reductive glutamine metabolism as evidenced by enrichment in malate and fumarate (m+3) isotopomers, relative to the control, which was abrogated by lapatinib (Figures 2E and S2M). Comparable effects of the KI/phenformin combinations on glucose uptake, and the lactate/pyruvate and α-KG/citrate ratios, were observed across all cancer cell lines (Figures 2F–2H and S2N). These data suggest that KIs may hinder metabolic adaptations to

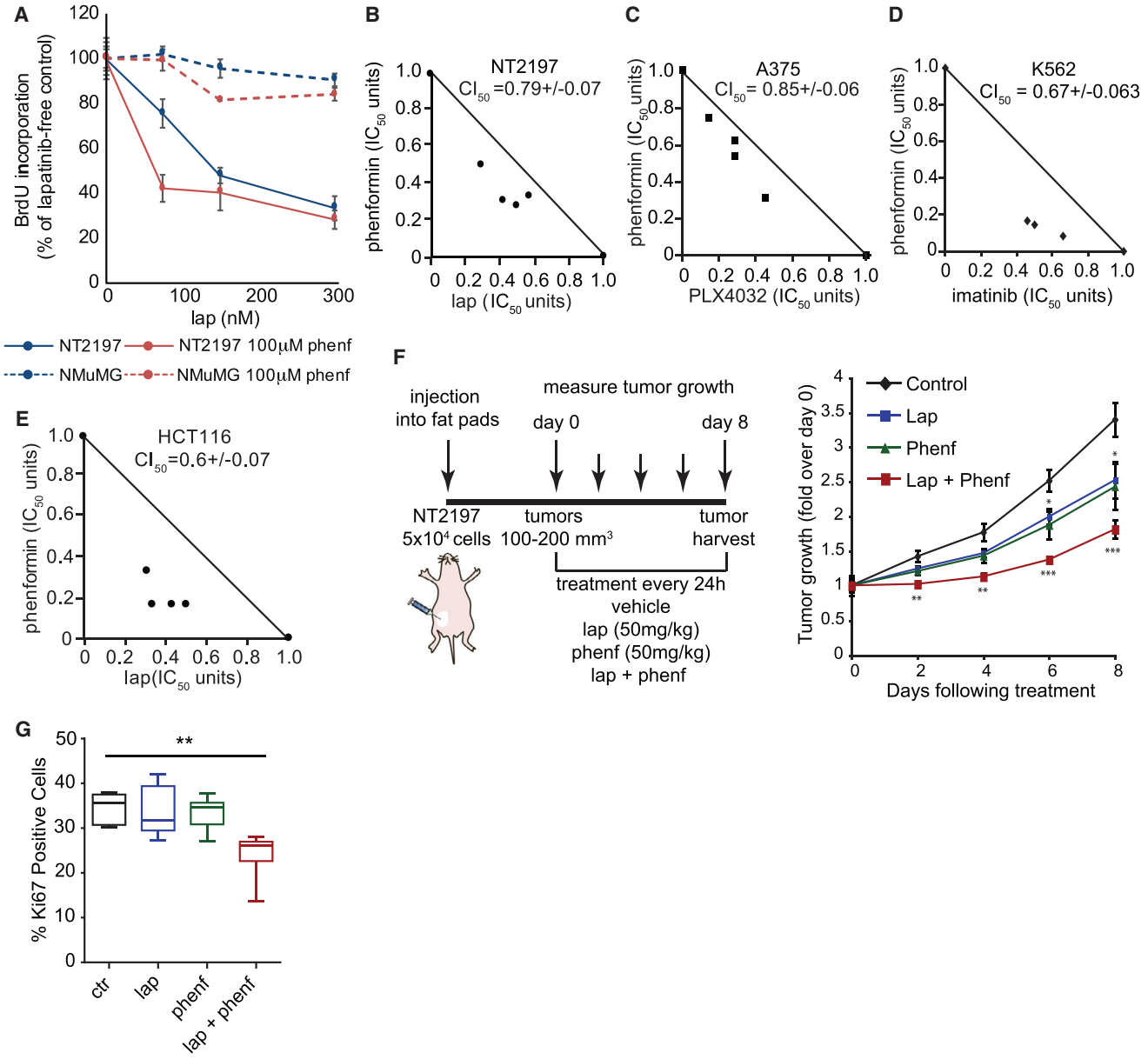

Figure 1. KIs and Phenformin Synergistically Inhibit Cell Proliferation and Suppress Tumor Growth *In Vivo*

(A) NMuMG and NT2197 cells were treated as indicated for 72 hr, and proliferation was monitored by BrdU incorporation and expressed as a percentage of non-lapatinib-treated cells.

(B) Combination index 50 (CI_{50}) for lapatinib and phenformin was determined by isobologram method (corresponding proliferation curves are shown in A and Figures S1C–S1E).

(C–E) A375 (C), K562 (D), and HCT116 (E) cells were treated with phenformin and/or PLX4032 (C), imatinib (D), or lapatinib (E), as indicated for 72 hr. Proliferation was estimated by BrdU incorporation. PLX4032 (C), imatinib (D), or lapatinib (E) interactions with phenformin were evaluated by the isobologram method. Corresponding proliferation curves are shown in Figures S1M–S1R, S2A, and S2B, and F and G.

In (A)–(E), the data are presented as means ± SD (three independent experiments, three technical replicates averaged in each).

(F and G) A total of 50,000 NT2197 cells were injected into two mammary fat pads of Nu/Nu mice. When tumors reached 100–200 mm^3, mice were randomly distributed into 4 groups of 5 mice and treated with phenformin (50 mg/kg), lapatinib (50 mg/kg), or both every 24 hr for 8 days. (F) Tumor growth was measured as described (Ursini-Siegel et al., 2007) every 2 days until the control tumors reached 500 mm^3. The data are presented as means ± SEM (n = 10 tumors) (*$p < 0.05$, **$p < 0.01$, and ***$p < 0.001$, two-way ANOVA). Mice were sacrificed on day 8, 4 hr after the last treatment. (G) Tumor sections from seven tumors/group were stained with Ki67 antibody. (**$p < 0.001$, ANOVA). Representative images are shown in Figure S2I.

See also Figures S1 and S2.

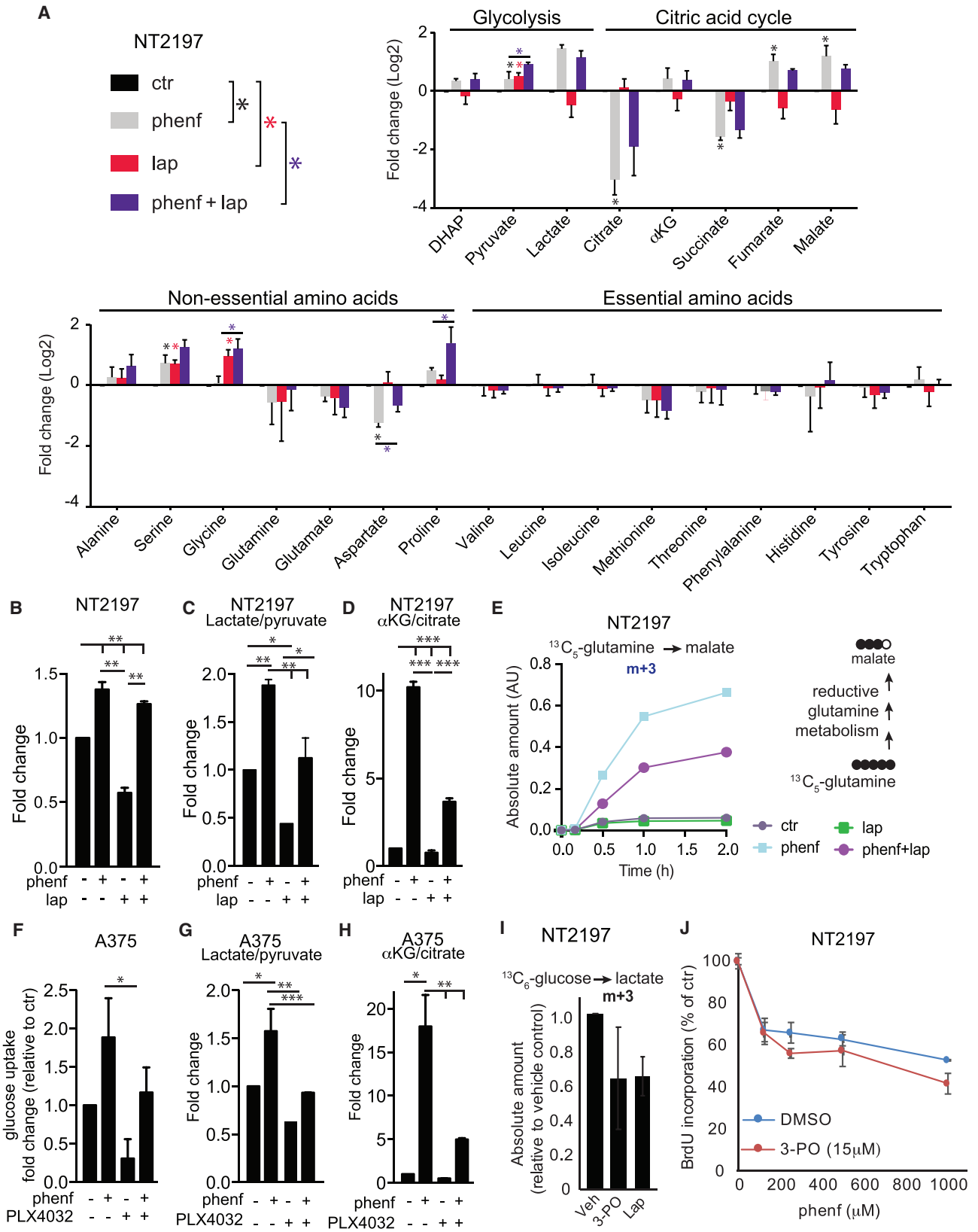

(legend on next page)

phenformin-induced energy stress by interfering with the reductive glutamine metabolism. Accordingly, depletion of isocitrate dehydrogenase 1 (IDH1), a rate-limiting reductive glutamine metabolism enzyme, potentiated the effects of the drug combination (Figure S2O).

Similar to the effects observed in tissue culture, phenformin increased lactate production and decreased citrate levels *in vivo* as compared to the control, whereas these effects were attenuated by lapatinib (Figure S2P). The magnitude of the *in vivo* effects was less than that in cell culture. This is consistent with lower achievable concentrations of phenformin *in vivo* as compared to cell culture (Table S1) and the presence of non-cancerous cells in tumors (e.g., fibroblasts), which are expected to be less affected by drugs (as shown for non-transformed cells in Figures 1A and S1F–S1J). Phenformin also increased glutamine levels in the tumors as compared to control and lapatinib (Figure S2P). In cell culture, observed responses to KIs and biguanides were associated with changes in glutamine metabolism; however, the role of glutamine utilization *in vivo* has been questioned (Davidson et al., 2016). To address this, mice bearing tumors were infused with $^{13}C_5$-glutamine (2 hr), leading to ~35% ^{13}C-labeled/total glutamine pool in tumors (Figures S2Q, S3A, and S3B). The metabolites derived from glutamine (glutamate, α-KG, citrate, malate, and succinate) incorporated ^{13}C at a considerable proportion of total pool (~20%–26%) (Figures S2Q, S3A, and S3B). Indeed, out of the total $^{13}C_5$-glutamine-labeled carbons present in the tumors, 79% ^{13}C were incorporated into glutamate, ~81% into citrate, ~67% into α-KG, and ~62% into malate and succinate, indicating that glutamine is an important anaplerotic source for CAC in NT2197 model.

Opposing Effects of Lapatinib and Phenformin on Glycolysis Are Insufficient to Explain Their Synergy

Suppression of the compensatory increase in glycolysis induced by biguanides has been reported to result in cell death (Ben Sahra et al., 2010). It is therefore plausible that lapatinib synergizes with phenformin by suppressing glucose uptake and/or glycolysis. We thus investigated the effects of combining phenformin with 3PO, which inhibits 6-phosphofructo-2-kinase/fructose-2,6-bisphosphatase 3 (PFKFB3) (Clem et al., 2008). 3PO was used instead of more potent glycolytic inhibitors (e.g., 2-DG) to induce a comparable suppression of glucose uptake and lactate production as lapatinib (~30%; Figures 2I, S3C, and S3D). Surprisingly, a 3PO concentration that inhibited glycolysis to a level comparable to lapatinib failed to synergize with phenformin (Figures 1B, 2J, S3E, and S3F). This suggests that lapatinib-induced inhibition of glycolysis cannot fully explain the lapatinib/phenformin synergy.

KIs and Biguanides Suppress Protein Synthesis and Cooperatively Downregulate mTORC1

Oncogenic kinases alter mRNA translation (Bhat et al., 2015). Since translation is highly energy demanding (Buttgereit and Brand, 1995), cancer cells must balance ATP production with translation rates (Morita et al., 2013). Indeed, sustained translation in energy-deficient cells is deleterious (Leprivier et al., 2013). Phenformin (250 μM) suppressed translation more strongly than lapatinib (600 nM) as illustrated by reduced polysome/monosome ratio and lower puromycilation (Figures S3G–S3I). The drug combination only marginally reduced translation as compared to phenformin alone (Figures S3G–S3I). This diminishes the plausibility that lapatinib/phenformin synergy is caused by energy depletion induced by sustained translation when ATP is limited.

The mechanistic/mammalian target of rapamycin complex 1 (mTORC1) stimulates translation (Bhat et al., 2015). Both lapatinib and phenformin inhibit mTORC1 (Bhat et al., 2015). We therefore determined the effects of lapatinib, phenformin, or combination thereof on mTORC1 signaling in NT2197 cells. Lapatinib (600 nM) abolished the MAPK/ERK signaling as evidenced by reduction in ERK1/2 phosphorylation relative to control, and suppressed mTORC1 as illustrated by decreased phosphorylation of the eukaryotic translation initiation factor 4E-binding protein 1 (4E-BP1) and the ribosomal protein S6 kinases 1 and 2 (S6K1/2), as well as ribosomal protein S6 (rpS6) (Figure 3A) (Bhat et al., 2015). Phenformin (250 μM) induced AMP-activated protein kinase (AMPK) and its downstream substrate acetyl-CoA carboxylase (ACC) (Munday, 2002) (Figure 3A). When the drugs were combined at concentrations

Figure 2. Kinase Inhibitors Oppose Phenformin-Induced Metabolic Changes

(A) Levels of indicated metabolites in NT2197 cells treated for 24 hr with phenformin (600 μM), lapatinib (600 nM), or combination thereof were determined by gas chromatography-mass spectrometry (GC-MS). Data are shown as mean ± SD. *p < 0.05 (two-way ANOVA; two independent experiments, three technical replicates averaged in each).

(B–D) NT2197 cells were treated with vehicle (DMSO), phenformin (250 μM), and/or lapatinib (600 nM) for 24 hr. (B) Glucose uptake was monitored by subtracting glucose concentration in media with cells versus cell-free media and normalized to DMSO control. Data are shown as mean ± SD. **p < 0.01 (two-way ANOVA; two independent experiments, three technical replicates averaged in each). (C and D) Intracellular lactate/pyruvate (C) and α-KG/citrate ratios (D) were determined by GC-MS and normalized to control. Data are shown as mean ± SD. *p < 0.05, **p < 0.01, and ***p < 0.001 (two-way ANOVA; two independent experiments, three technical replicates averaged in each).

(E) NT2197 cells were treated as in (B)–(D) for 24 hr and incubated with $^{13}C_5$-glutamine. Absolute malate (m+3) ion levels are shown. Data are representative of two independent experiments. AU, arbitrary units. Right: schematic of the ^{13}C incorporation into metabolites.

(F–H) A375 cells were treated with phenformin (1.5 mM) and/or PLX4032 (200 nM) for 24 hr. (F) Glucose uptake was normalized to DMSO control. Data are shown as mean ± SD. *p < 0.05 (two-way ANOVA; three independent experiments, three averaged technical replicates each). (G and H) Intracellular lactate/pyruvate (G) and α-KG/citrate (H) ratio. Metabolites were measured by GC-MS and normalized to DMSO control. Data are shown as mean ± SD. *p < 0.05, **p < 0.01, and ***p < 0.001 (two-way ANOVA; two independent experiments, three technical replicates averaged in each).

(I) NT2197 cells treated with vehicle (DMSO), 3-PO (15 μM), or lapatinib (300 nM) for 24 hr were incubated with $^{13}C_6$-glucose for 90 min. Absolute lactate (m+3) ion amounts are shown, normalized to control. Data are shown as mean ± SD from three independent experiments.

(J) NT2197 cells were treated as indicated for 72 hr. Proliferation was monitored by BrdU incorporation and expressed as percentage of non-phenformin treated cells. The data are presented as mean ± SD (two independent experiments, three technical replicates averaged in each).

See also Figures S2 and S3.

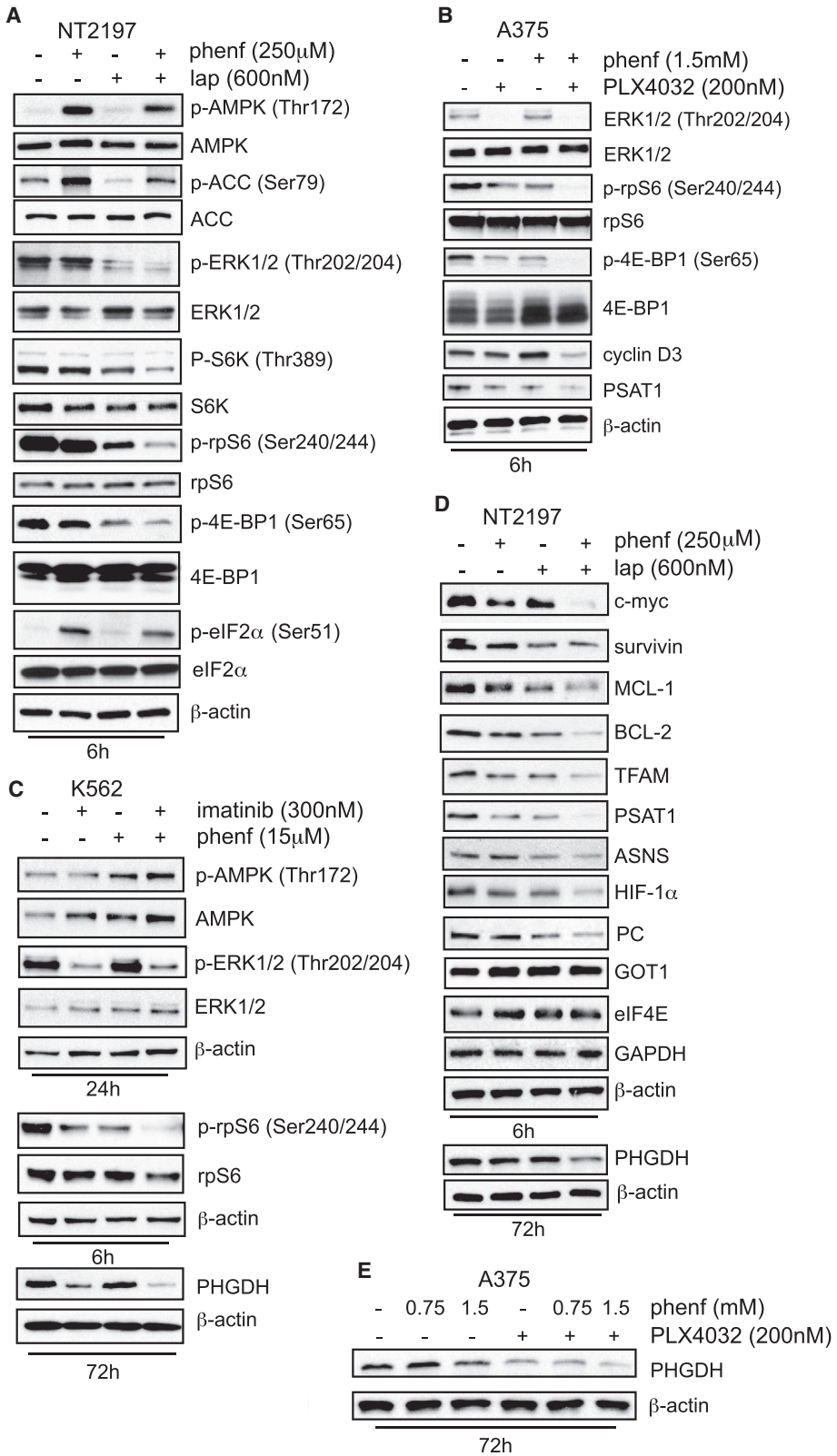

Figure 3. Kinase Inhibitors and Phenformin Collaboratively Inhibit mTORC1

NT2197 (A and D), A375 (B and E), and K562 (C) cells were treated as indicated. Levels and phosphorylation status of indicated proteins were determined using western blot. β-actin was a loading control. These data are representative of at least two independent replicates.

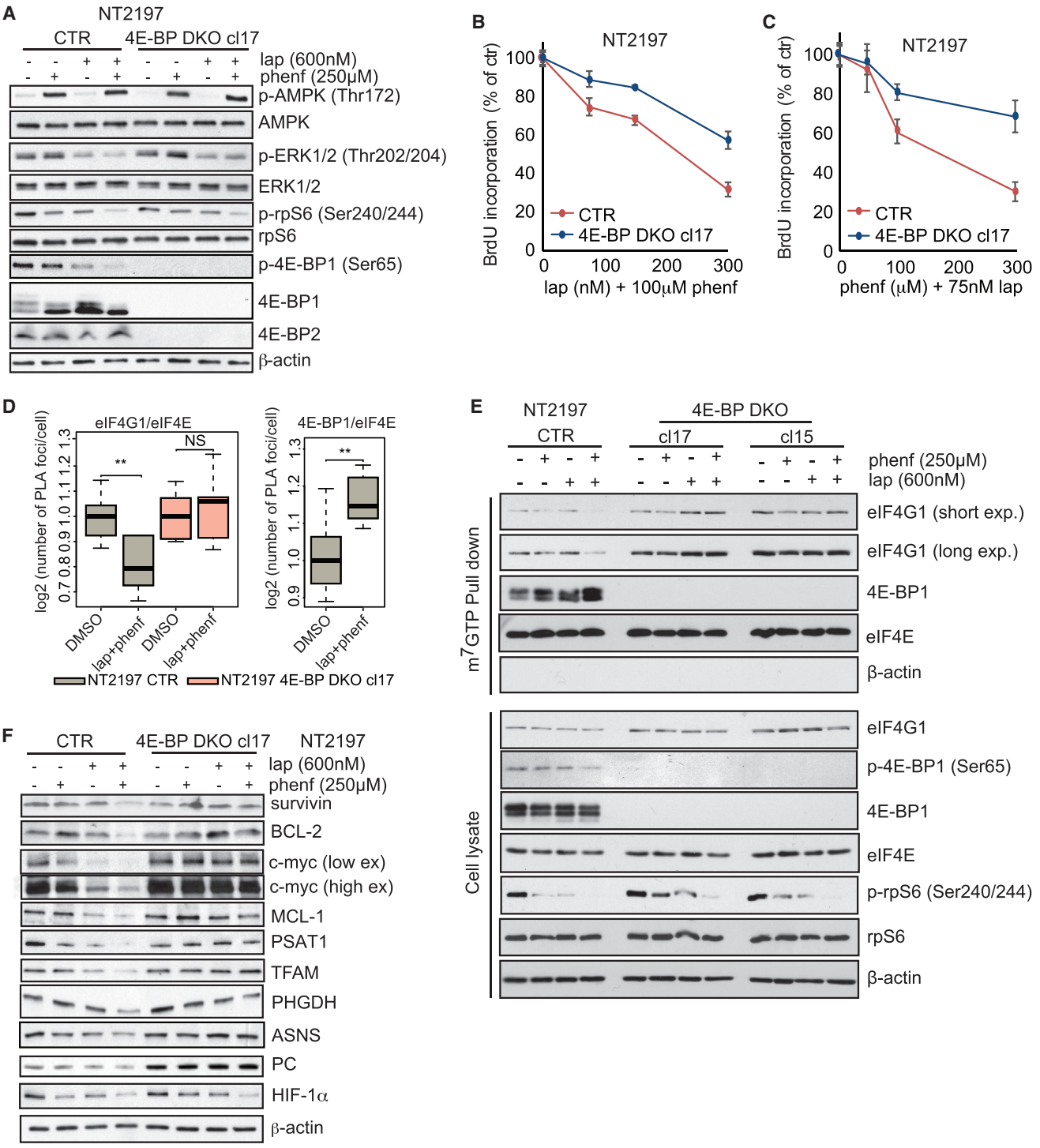

Figure 4. 4E-BP1/2 Determine the Efficacy of the Lapatinib/Phenformin Combination

(A) Control (CTR) or CRISPR 4E-BP1 and 2 depleted (4E-BP DKO clone 17; cl17) NT2197 cells were treated as indicated for 6 hr. The expression and phosphorylation status of indicated proteins were determined by western blot. β-actin was a loading control. Data are representative of two independent replicates.

(B and C) CTR or 4E-BP DKO cl17 NT2197 cells were treated as indicated for 72 hr. Proliferation was monitored by BrdU incorporation and was expressed as a percentage of vehicle (DMSO)-treated cells. The data are presented as mean ± SD (three independent experiments, three technical replicates averaged in each).

(D and E) CTR or indicated clones of 4E-BP DKO NT2197 cells were treated with phenformin (250 μM), lapatinib (600 nM), or combination thereof for 4 hr. The interactions between eIF4E/eIF4G1 and eIF4E/4E-BP1 were assessed by proximity ligation assay (D) and m^7GDP pull-down (E). (D) **$p < 0.001$ (ANOVA; post hoc

(legend continued on next page)

that result in synergistic effects, mTORC1 was suppressed to a higher extent relative to each drug alone (Figures 3A and S3J). Similar effects of KI/phenformin combinations on signaling were observed *in vivo* (Figure S3K) and other cancer types (Figures 3B and 3C).

The phenformin/lapatinib combination suppressed mTORC1 and translation to a lesser extent than mTOR inhibitor torin1 (Figures S3I and S3L). The moderate mTORC1 inhibition by the phenformin/lapatinib combination, however, was associated with a pronounced pro-apoptotic effect, whereas almost complete obliteration of mTORC1 signaling with torin1 led to a mostly cytostatic effect (Figure S1L). This is consistent with the tenet that potent mTOR inhibitors (e.g., torin1) induce metabolic dormancy, where suppression of ATP production is compensated by reduction in translation and other anabolic processes, thus leading to reduced ATP consumption (Gandin et al., 2016b; Morita et al., 2013). Phenformin/lapatinib synergy is therefore not attributable solely to mTORC1 inhibition, but it appears to be mediated by moderate mTORC1 suppression in concert with metabolic stress.

eIF2α phosphorylation leads to reduced protein synthesis (Ron and Harding, 2007). Phenformin, but not lapatinib, stimulated eIF2α phosphorylation (Figure 3A), consistent with the more pronounced inhibition of global translation by phenformin than lapatinib (Figures S3G–S3I). Thus, in addition to their opposing effects on glycolysis and reductive glutamine metabolism, lapatinib and phenformin cooperatively suppress mTORC1, which, in addition to the induction of eIF2α phosphorylation by phenformin, results in decreased protein synthesis.

4E-BPs Are Essential for Synergistic Effects of KI and Biguanides

In addition to regulating global translation, mTOR selectively perturbs the translatome (Bhat et al., 2015). This is in part mediated by the effects of mTORC1 on 4E-BPs and, consequently, on the eIF4F complex assembly (Bhat et al., 2015). KI/phenformin combination reduced the levels of proteins encoded by mRNAs previously demonstrated to be ''eIF4F-sensitive'' more dramatically than either drug alone. These included anti-apoptotic proteins (survivin, MCL-1, and BCL-2), oncogenes (c-MYC), and factors with mitochondrial functions (TFAM), but not those whose expression is less ''eIF4F-sensitive'' (β-actin, GAPDH, GOT1, or eIF4E; Figures 3B–3E).

To investigate whether the mTORC1/4E-BP/eIF4F axis contributes to lapatinib/phenformin synergy, we generated NT2197 cells that lack 4E-BP1 and 2 by CRISPR/Cas9 (Figure 4A). 4E-BP1/2 loss decreased the anti-proliferative and pro-apoptotic effects of the lapatinib/phenformin combination relative to 4E-BP1/2-proficient cells (Figures 4B, 4C, and S4A–S4I) or 4E-BP1/2-deficient cells in which 4E-BP1 was re-expressed (Figures S4J and S4K). 4E-BP1/2 loss also negated the effects of the drug combination on the eIF4F complex assembly (Figures 4D, 4E, S4L, and S5A; Data S1). This was paralleled by diminished effects of the drugs on the levels of proteins encoded by ''eIF4F-sensitive'' mRNAs (Figure 4F). The loss of 4E-BP1/2 also attenuated the anti-proliferative effects of the PLX4032/phenformin combination in A375 cells (Figures S4M and S4N). These findings show that 4E-BPs are critical for KI/biguanide synergy.

The mTORC1/4E-BP Axis Regulates Translation of mRNAs Encoding Rate-Limiting Enzymes of Metabolic Pathways that Fuel Neoplastic Growth, Including NEAA Synthesis

Serine, aspartate, and asparagine biosynthesis pathways are implicated in mTOR-driven oncogenesis (DeBerardinis and Chandel, 2016; Vander Heiden and DeBerardinis, 2017). Relative to single drugs, KI/phenformin combinations decreased levels of proteins that play key roles in these metabolic pathways, including phosphoglycerate dehydrogenase (PHGDH), phosphoserine aminotransferase 1 (PSAT1), pyruvate carboxylase (PC), and asparagine synthetase (ASNS), but not glutamic-oxaloacetic transaminase 1 (GOT1) (Figures 3B–3E, and S4N). Ablation of 4E-BP1/2 abolished the effects of drug combinations on the expression of these proteins (Figures 4F and S4N).

We next assessed whether the observed effects of the lapatinib/phenformin combination occur at the level of translation by polysome profiling (Gandin et al., 2014) (Figure 5A). In NT2197 cells, under basal conditions, *Phgdh*, *Psat1*, *Pc*, and *Asns* mRNAs are translated at high efficiency as illustrated by their distribution within the heavy polysome fractions (Figure 5B). The lapatinib/phenformin combination reduced translation of *Phgdh*, *Psat1*, *Pc*, and *Asns* mRNAs in 4E-BP1/2 proficient, but not deficient, cells, as evidenced by their shift toward the fractions with less ribosomes (Figure 5B). A similar trend was observed for *Ccnd3* mRNA, which is regulated via the mTORC1/4E-BP pathway (Larsson et al., 2012). In contrast, lapatinib and phenformin only marginally affected translation of ''eIF4F-insensitive'' *Actb*, *Gapdh*, or *Got1* mRNAs (Figure 5B). These changes were not accompanied by changes in *Phgdh*, *Psat1*, and *Asns* mRNA levels, whereas *Pc* mRNA was slightly increased in 4E-BP1/2-deficient versus -proficient cells (Figures S5B and S5C). These data demonstrate that the mTORC1/4E-BP-dependent translation control may play a role in serine, aspartate, and asparagine synthesis.

Metabolic Reprogramming Caused by 4E-BP1/2 Loss Decreases the Efficacy of the KI/Biguanide Combinations

4E-BP1/2 status in the cells determines translation of mRNAs encoding proteins that play critical roles in aspartate, asparagine, and serine synthesis (Figure 5B) and mitochondrial functions (Gandin et al., 2016b; Morita et al., 2013). Accordingly, amino acids, including aspartate, asparagine, serine, and alanine, as well as CAC intermediates (e.g., malate, fumarate, and succinate) and pyruvate, were elevated in

Tukey test from ten different fields). Representative images are shown in Figure S5A and Data S1. (E) Amounts of the indicated proteins in the input or pull-down were determined by western blot; β-actin was a loading control (input) and was used to exclude contamination (m^7GDP pull-down).
(F) CTR or 4E-BP DKO cl17 cells were treated as shown. The expression of indicated proteins was determined by western blot. β-actin was a loading control.
(E and F) Experiments are representative of two independent replicates.
See also Figures S4 and S5.

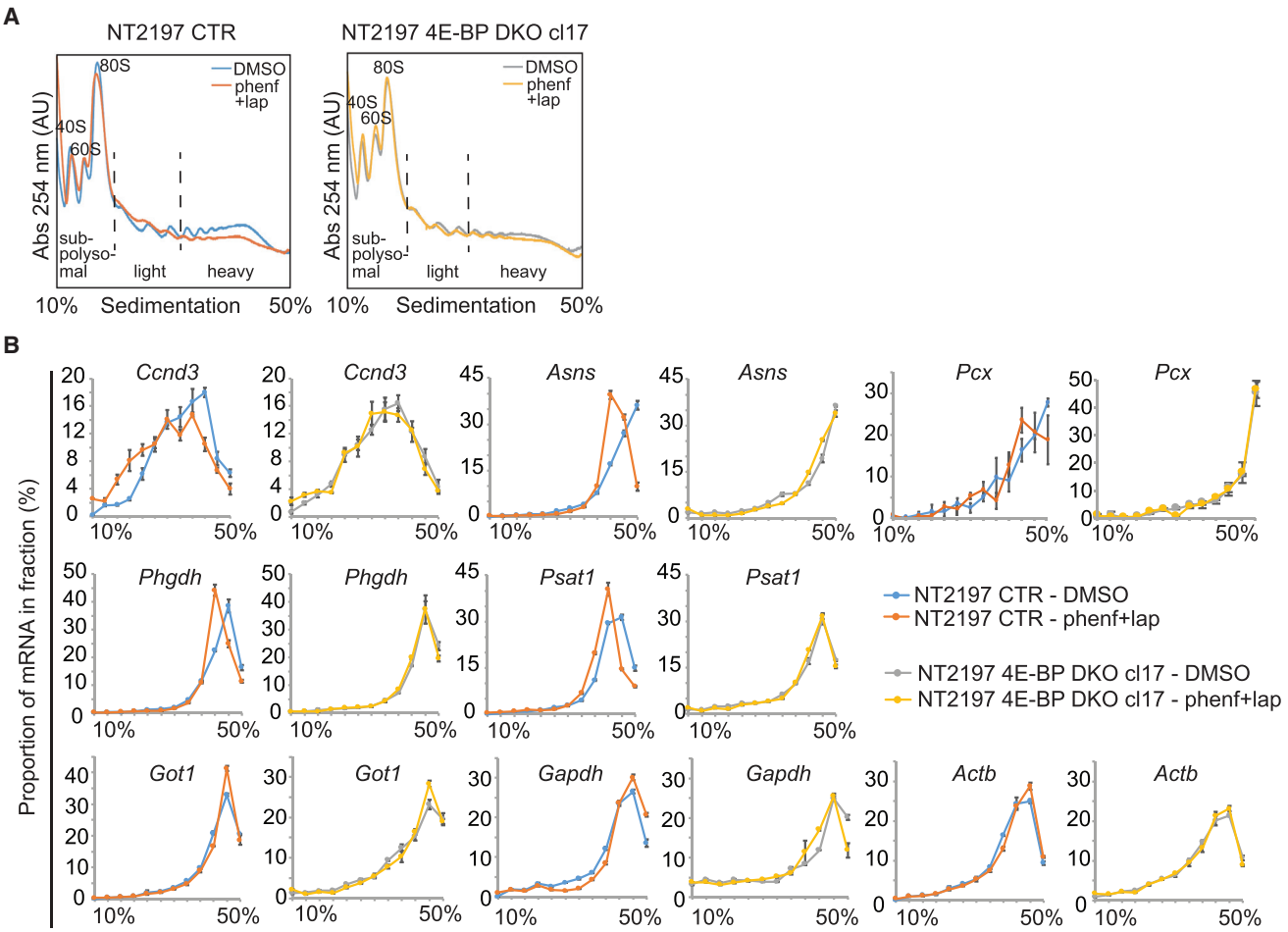

Figure 5. Phenformin/Lapatinib Combination Suppresses Translation of mRNAs that Encode NEAA Biosynthetic Enzymes

(A) CTR or 4E-BP DKO cl17 NT2197 cells were treated with vehicle (DMSO) or combination of phenformin (250 μM) and lapatinib (600 nM) for 4 hr. Sub-polysomal, light-, and heavy-polysome fractions were obtained by ultracentrifugation using 5%–50% sucrose gradients. Positions of 40S and 60S ribosomal subunits, monosome (80S), and polysomes in the absorbance profiles (254 nm) are shown.

(B) Amount of indicated mRNAs in polysome fractions was determined by qRT-PCR (as described; Miloslavski et al., 2014). Corresponding total mRNA levels are shown in Figures S5B and S5C. Data are representative of three independent experiments (three technical replicates each) and are expressed as a percentage of mRNA in each fraction ± SD.

See also Figure S5.

4E-BP1/2-deficient versus -proficient cells (Figures 6A and S5D). Combining phenformin and lapatinib altered the levels of these metabolites in both control and 4E-BP1/2 NT2197 knockout (KO) cells, but their abundance remained significantly higher in cells lacking 4E-BP1/2 (Figures 6A and S5D).

Aspartate and serine synthesis are involved in nucleotide and protein synthesis and other processes required for proliferation (Vander Heiden and DeBerardinis, 2017). To identify metabolic pathways responsible for the increase in aspartate in 4E-BP1/2 ablated cells, we performed $^{13}C_6$-glucose tracing. 4E-BP1/2 loss increased the proportion of m+3 aspartate, malate, and fumarate, as compared to control (Figure S5E), as well as the absolute amount of m+3 aspartate and malate (Figures 6B and S6A). Thus, cells lacking 4E-BP1/2 maintain high aspartate levels by using pyruvate to generate malate and aspartate via oxaloacetate (Figures S5E and S6A), which is consistent with elevated PC levels (Figure 4F). This finding was confirmed by higher 3-^{13}C-glucose-derived m+1 aspartate levels in 4E-BP1/2-depleted versus control cells (Figure S6B). Importantly, 10 mM aspartate decreased sensitivity of control cells to the drug combination (Figure 6C), whereas it only marginally influenced the drug efficacy in 4E-BP1/2-deficient cells in which aspartate levels are already high (Figure S6C). Aspartate is essential for *de novo* synthesis of asparagine, which is catalyzed by asparagine synthetase (ASNS) that simultaneously converts glutamine to glutamate (Balasubramanian et al., 2013). Consistent with mTORC1/4E-BP-dependent regulation of ASNS (Figures 3D, 4F, and 5B), cells lacking 4E-BP1/2 exhibit higher asparagine and glutamate levels than control cells (Figure 6A). Asparagine also alleviated the anti-proliferative effects of the drug combination in 4E-BP1/2-proficient cells (Figure 6D). This suggests that the effects of aspartate may be mediated by its conversion to asparagine. Indeed, ASNS depletion increased the phenformin/lapatinib combination efficacy (Figures S6D–S6F). Finally,

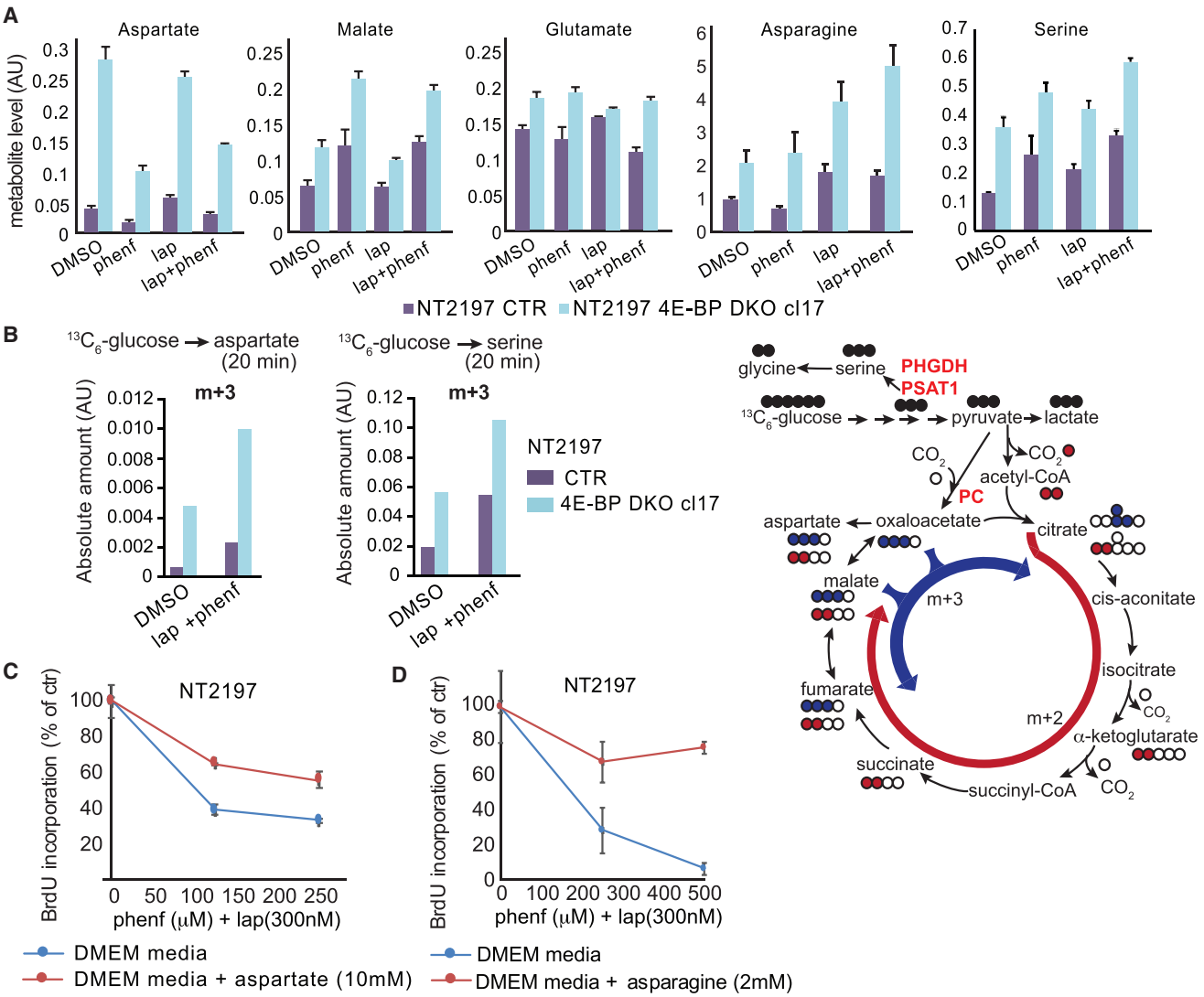

Figure 6. 4E-BP1/2 Determine the Lapatinib/Phenformin Combination Efficacy

(A) Control (CTR) or 4E-BP DKO cl17 NT2197 cells were treated with phenformin (250 μM), lapatinib (600 nM), or combination thereof for 24 hr. Levels of indicated metabolites were determined by GC-MS. Additional metabolites are shown in Figure S5D. Data represent means ± SD (two independent experiments, three technical replicates averaged in each).

(B) Cells from (A) were incubated with $^{13}C_6$-glucose for 20 min. Stable isotope tracer analyses were performed and the absolute levels of aspartate (m+3) and serine (m+3) ions are shown. Data are representative of two independent experiments. AU, arbitrary units. More isotope tracing data are shown in Figure S5E. Right: schematic of the ^{13}C incorporation into metabolites.

(C and D) NT2197 CTR cells were treated as indicated for 72 hr. Where indicated media were supplemented with aspartate (10 mM) (C) or asparagine (2 mM) (D). Proliferation was monitored by BrdU incorporation and expressed as a percentage of control treated cells. The data are presented as means ± SD (two independent experiments, three technical replicates averaged in each).

See also Figures S5 and S6.

depletion of asparagine from media by L-asparaginase potentiated effects of phenformin/lapatinib combination to a greater extent in 4E-BP-proficient than 4E-BP-deficient cells (Figure S6G). Serine levels and the proportion of m+3 serine derived from $^{13}C_6$-glucose are higher in 4E-BP-deficient versus -proficient cells (Figures 6A, 6B, and S5E), which is consistent with 4E-BP-mediated effects of the drug combination on PHGDH and PSAT1 levels. Serine has been shown to influence sensitivity to biguanides (Gravel et al., 2014). Accordingly, depletion of PHGDH in 4E-BP1/2-deficient cells increased drug combination efficacy (Figures S6H–S6J). Thus, mTORC1/4E-BP-mediated effects on aspartate, asparagine, and serine biosynthesis determine the efficacy of the KI/biguanide combinations.

HIF-1α Influences Sensitivity to Lapatinib and Phenformin

HIF-1α is upregulated in HER2 overexpressing cells (Schito and Rey, 2017). In NT2197 cells, the phenformin/lapatinib combination more strongly decreased HIF-1α than single drugs (Figure 3D), which was paralleled by the reduction of HIF-1α target

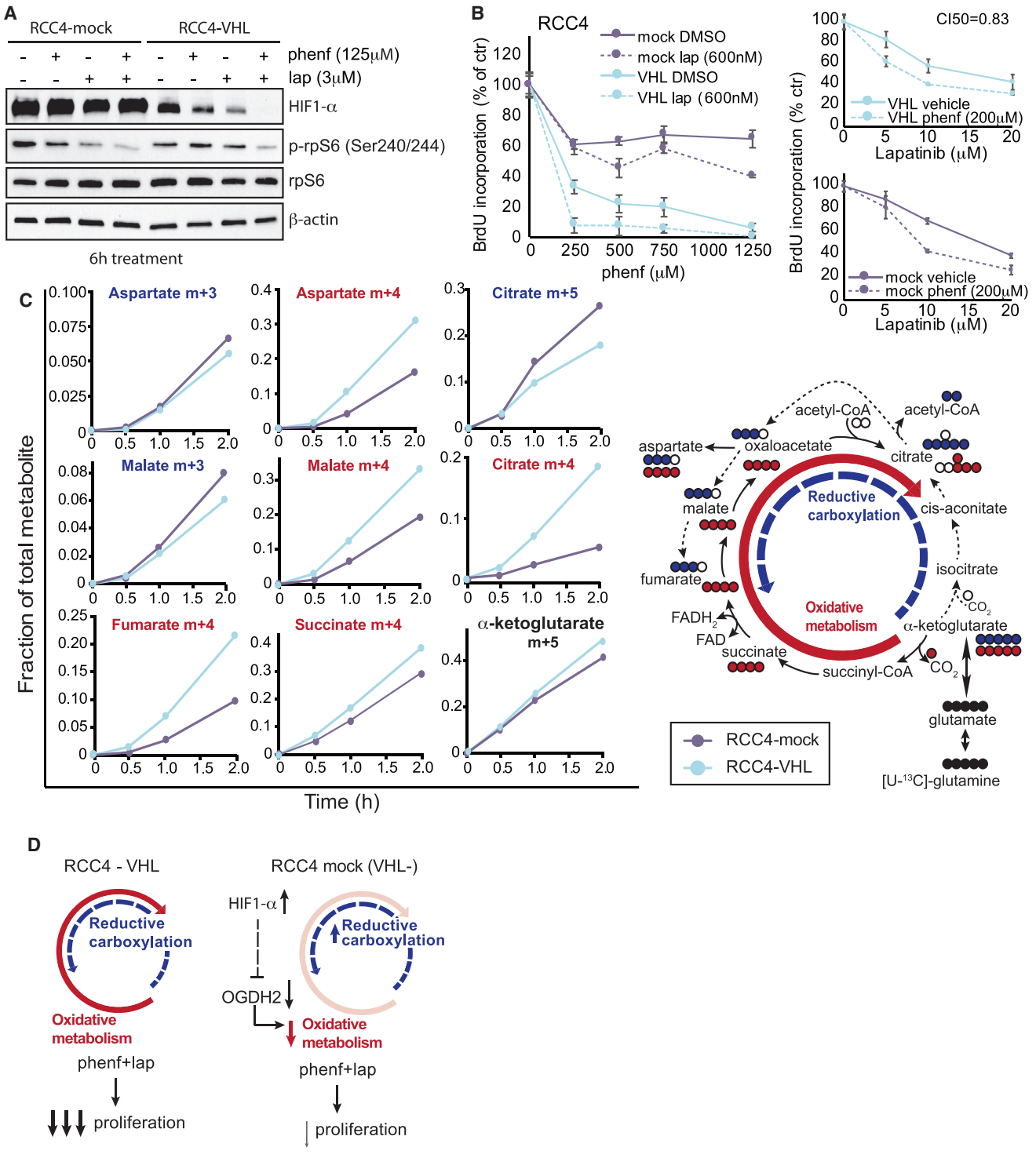

Figure 7. The Phenformin/Lapatinib Combination Efficacy Is Influenced by HIF-1α

(A) VHL null RCC4 cells expressing either empty vector (RCC4-mock) or VHL (RCC4-VHL) were treated as shown for 6 hr. Expression of indicated proteins was determined by western blot. β-actin was a loading control (representative data from two independent experiments).

(B) Cells from (A) were treated with the indicated concentration of phenformin and lapatinib for 72 hr. Proliferation was monitored by BrdU incorporation and was expressed as a percentage of vehicle (DMSO)-treated cells. The data are presented as means ± SD (three independent experiments, three technical replicates averaged in each).

(legend continued on next page)

genes (Figure S6K). Of note, *Vegfa*, *Glut1*, and *Hk2* mRNAs were decreased by lapatinib alone (Figure S6K), which is consistent with previous observations (Acharya et al., 2016; Le et al., 2008; Liu et al., 2016). In turn, HIF-2α was undetectable under normoxic conditions (Figure S6L), which can be explained by differential regulation of HIF-1α and 2α by HER2 (Whelan et al., 2013).

mTOR regulates HIF-1α by multiple mechanisms including via 4E-BPs (Dodd et al., 2015). In NT2197 cells, however, HIF-1α does not appear to be regulated by 4E-BPs (Figure 4F). E3 ubiquitin ligase VHL regulates expression of HIFs by degrading them under normoxia (Semenza, 2007). RCC4 renal carcinoma cells lack VHL and express high levels of HIF-1α (Maxwell et al., 1999). Notably, lapatinib has been used in renal cancer clinical trials (Ravaud et al., 2008). The lapatinib/phenformin combination reduced HIF-1α in VHL-reconstituted (RCC4-VHL), but not VHL null, RCC4 cells (RCC4-mock) (Figure 7A). This effect was abolished by hypoxia-mimetic $CoCl_2$ (Figure S6M). VHL status did not influence the effects of the drugs on mTORC1 (Figure 7A). Thus, the lapatinib/phenformin combination reduces HIF-1α levels in RCC4 cells in a VHL-dependent manner. Accordingly, the anti-proliferative effect of the drug combination was less pronounced in RCC4-mock versus RCC4-VHL cells (Figures 7B and S7A). This suggests that downregulation of HIF-1α critically contributes to lapatinib/biguanide synergy. Indeed, stabilization of HIF-1α with dimethyloxallyl glycine (DMOG) (Cummins et al., 2008) decreased sensitivity of the RCC4-VHL cells to the drug combination (Figures S7B and S7C). Notwithstanding that DMOG concentrations used for acute HIF-1α stabilization range between 250 and 1,000 μM (Heir et al., 2016), for the proliferation assay we used 25 μM DMOG, which is sufficient to stabilize HIF-1α levels without toxicity during a 72 hr treatment (Figures S7B and S7C).

Phenformin induced glycolysis in both RCC4-mock and RCC4-VHL cells, as monitored by the lactate/pyruvate ratio; however, the magnitude of the effects was greater in RCC4-VHL cells, and this was impeded by lapatinib (Figure S7D). Loss of VHL triggers reductive glutamine metabolism (Gameiro et al., 2013), which was confirmed by $^{13}C_5$-glutamine tracing that revealed higher levels of citrate (m+5), malate (m+3), and aspartate (m+3) isotopomers in RCC4-mock versus RCC4-VHL cells (Figures 7C and S7E). Conversely, lower levels of oxidative glutamine metabolism-derived fumarate (m+4), malate (m+4), aspartate (m+4), and citrate (m+4) isotopomers were observed in RCC4-mock versus RCC4-VHL cells (Figure 7C). These findings suggest that HIF-1α-dependent regulation of reductive glutamine metabolism determines the effects of phenformin/lapatinib combination (Figure 7D). We therefore induced HIF-1α levels in RCC4-VHL cells with DMOG (Figure S7C) followed by $^{13}C_5$-glutamine tracing. DMOG increased markers of reductive (citrate m+5, isocitrate m+5), while decreasing oxidative (citrate m+4, isocitrate m+4) glutamine metabolism intermediates, relative to vehicle-treated cells (Figure S7F). Since DMOG may induce metabolic effects before affecting HIF-1α levels (Zhdanov et al., 2015), we depleted HIF-1α in RCC4-mock cells, which resulted in an increase in oxidative and a decline in reductive glutamine metabolism (Figures S7G and S7H). Consistently, viability of RCC4-mock cells was decreased upon suppression of reductive glutamine metabolism by IDH1 depletion, which was further potentiated by the drug combination (Figure S7I). Untreated RCC4-VHL cells were only marginally affected by IDH1 depletion, which is in accordance with their preference for oxidative glutamine metabolism. In contrast, the effects of the phenformin/lapatinib combination on viability were potentiated by IDH1 depletion in RCC4-VHL cells (Figure S7I). HIF-1α negatively affects mitochondrial enzyme complex α-ketoglutarate dehydrogenase (αKGDH) subunit E1 (OGDH) (Sun and Denko, 2014). OGDH catalyzes the oxidative decarboxylation of α-KG to succinyl-CoA. At baseline, OGDH levels were lower in VHL-deficient versus -proficient RCC4 cells (Figure S7J), which was mirrored by alterations in the $^{13}C_5$-glutamine-derived succinate (m+4) (Figures 7C and 7D). Moreover, the phenformin/lapatinib combination decreased OGDH levels in VHL-proficient, but not -deficient, cells (Figure S7J), which is consistent with the drugs acting via HIF-1α. HIF-2α levels were higher in RCC4-mock as compared to RCC4-VHL cells, but HIF-2α protein levels were not affected by drugs (Figure S7K). These findings demonstrate that HIF-1α-dependent modulation of glutamine metabolism is a critical determinant of the efficacy of KI/biguanide combinations.

DISCUSSION

It has been proposed that biguanides may improve KI efficacy. Preclinical studies suggest that biguanides enhance activity of trastuzumab, BRAF, and ERK inhibitors (Trousil et al., 2017; Vazquez-Martin et al., 2011; Yuan et al., 2013). Although these findings are being evaluated in clinical trials, the underlying mechanisms are not fully understood. We show that KIs synergize with biguanides in cancer cell types that differ in their origin and the driving oncogenic kinase. KIs attenuate the biguanide-induced increase in glycolysis, which was considered as a plausible mechanism to account for the synergy between the drugs. However, our data show that this simple model is insufficient to explain KI/biguanide synergy. We show that metabolic and translational perturbation mediated via the mTORC1/4E-BP1 axis and HIF-1α critically contribute to the efficacy of KI/biguanide combinations.

Aspartate has been identified as a key metabolite required for neoplastic growth (Vander Heiden and DeBerardinis, 2017). Aspartate can be generated from pyruvate via PC, which converts pyruvate to oxaloacetate (Ling and Keech, 1966). Elevated PC expression and/or activity is observed in breast cancer and non-small-cell lung cancer (Phannasil et al., 2017; Sellers et al., 2015). We show that *Pc* mRNA translation is regulated via 4E-BPs and that 4E-BP1/2 ablation leads to dramatic increase in aspartate levels and reduction in sensitivity to the KI/phenformin

(C) Cells described in (A) were incubated with $^{13}C_5$-glutamine for 30 min, 1 hr, and 2 hr. Stable isotope tracer analysis was performed, and the levels of the indicated ion amounts (fraction of the total pool) are shown. Data are representative of two independent experiments. Bottom right panel: schematic of the ^{13}C incorporation into metabolites. For additional data, see Figure S7E.

(D) Schematic showing the utilization for glutamine in RCC4 cells depending on VHL status/HIF-1α levels.

See also Figures S6 and S7.

combination. GOT1 is required for aspartate synthesis under electron transport chain deficiency (Birsoy et al., 2015). The phenformin/lapatinib combination does not alter GOT1 (Figures 3D and 5B), suggesting the existence of an alternative mechanism whereby aspartate levels are influenced through the action of PC. Furthermore, aspartate conversion to asparagine, which is regulated by 4E-BP-dependent translation of *Asns* mRNA, appears to play a major role in the phenformin/KI synergy. Accordingly, L-asparaginase, which depletes asparagine pools, is used in treating low-ASNS-expressing acute lymphoblastic leukemia and pediatric acute myeloid leukemia (Hill et al., 1967). ASNS is also required for KRAS-driven oncogenesis (Gwinn et al., 2018); glioma, neuroblastoma, and mouse sarcoma growth (Hettmer et al., 2015; Zhang et al., 2014); and breast cancer metastasis (Knott et al., 2018).

Cancer cells exhibit increased serine biosynthesis (Snell, 1984). PHGDH and PSAT1 are overexpressed in subtypes of breast cancer, melanoma, cervical cancer, and glioma (DeBerardinis and Chandel, 2016) and are linked to poor prognosis in lung cancers (DeNicola et al., 2015; Zhang et al., 2017). Increase in serine synthesis appears to be beneficial for cancer cells irrespective of the availability of serine in the environment, or intracellular serine levels (Mattaini et al., 2016). This is explained by serine being a central node for the biosynthesis of many metabolites (e.g., nucleotides, folate metabolism), amino acid transport, and redox homeostasis (DeBerardinis and Chandel, 2016). Accordingly, we show that 4E-BP-dependent translational regulation of serine synthesis is a critical determinant of sensitivity of cancer cells to KI/biguanide combinations.

We also provide evidence suggesting that HIF-1α-dependent modulation of glutamine metabolism underpins the KI/phenformin synergy. HER2 upregulates HIF-1α, even under normoxic conditions (Semenza, 2013), which is required for neoplastic growth (Whelan et al., 2013). KI/biguanide combinations appear to downregulate HIF-1α via VHL, which is in accordance with reports showing that metformin induces HIF-1α degradation through inhibition of mitochondrial complex I (Wheaton et al., 2014). RCC4 cells that lack VHL and thus exhibit high HIF-1α are less sensitive to the KI/biguanide combination, which coincides with increased reductive glutamine metabolism (Sun and Denko, 2014). These data suggest that VHL loss and/or HIF-1α activation decreases the efficacy of KI/biguanide combinations. Therefore, the mTORC1/4E-BP and VHL/HIF-1α axes constitute two independent mechanisms that allow metabolic adaptations to KI/biguanide combinations.

Strong mTOR inhibition is associated with metabolic dormancy and cytostatic effects (Gandin et al., 2016b; Morita et al., 2013). In stark contrast, KI/biguanide combinations, although inducing considerably less inhibition of mTOR, result in cell death. Our findings therefore suggest that mild mTOR inhibition, which is sufficient to induce translational reprogramming of the metabolome, but not to decrease energy consumption, is more likely to lead to an energetic crisis and cell death than more potent mTOR inhibition. This suggests that targeting oncogenic mTOR signaling with combinations of upstream KIs and biguanides may be an alternative to mTOR inhibitors. However, it is important to note that early results of clinical trials employing biguanides in oncology have been disappointing (Kordes et al., 2015). One reason for this may relate to sub-optimal pharmacokinetics of metformin (Chandel et al., 2016; Dowling et al., 2016), an issue that may be addressed by the use of novel biguanides or other OXPHOS inhibitors (Molina et al., 2018; Zhang et al., 2016). Other trials, including one using phenformin in combination with BRAF inhibitors, are underway (https://clinicaltrials.gov/; NCT03026517). Our study shows that metabolic adaptations that underpin plasticity of cancer cells should also be considered as a factor explaining the potential limited clinical efficacy of biguanides, including KI/biguanide combinations.

In conclusion, we show that 4E-BP-dependent translational regulation of NEAA synthesis, in combination with HIF-1α-dependent alterations in glutamine metabolism, determines the efficacy of KI/biguanide combinations. This suggests that the outcomes of drug-induced energy stress depend on the ability of cancer cells to engage multiple pathways that underlie metabolic adaptations. Indeed, metabolic plasticity is emerging as a major factor in resistance to cancer treatments (Boudreau et al., 2016; Krstic et al., 2017; Lehuédé et al., 2016). Metabolic plasticity thus represents a paramount challenge, as genetic and/or epigenetic alterations, including those affecting 4E-BP and HIF-1α function, enable cancer cells to evade metabolic stresses and hinder efficacy of metabolome-focused cancer therapies. This suggests that further research should focus on identifying specific targets for which metabolic plasticity would have limited potential of attenuating drug efficacy.

Limitations of Study

This study unraveled the mechanisms of synergy between KIs and biguanides and identified metabolic plasticity as a major factor that determines their efficacy. Nonetheless, *in vivo* studies in relevant pre-clinical models are required to provide more clinical relevance (e.g., addressing issues related to pharmacokinetics and pharmacodynamics of the KI/biguanide combinations). Moreover, systems biology approaches are warranted to capture the full complexity of perturbations in gene expression and signaling networks that underpin the metabolic adaptability of tumors to therapeutic insults. Finally, future research is needed to determine the mechanisms of metabolic plasticity of neoplasia at the organismal level.

STAR★METHODS

Detailed methods are provided in the online version of this paper and include the following:

- KEY RESOURCES TABLE
- CONTACT FOR REAGENT AND RESOURCE SHARING
- EXPERIMENTAL MODEL AND SUBJECT DETAILS
  - Cell Lines and Cell Culture Conditions
- METHOD DETAILS
  - Generation of Knock-Down Cell Lines by shRNA
  - Generation of 4E-BP1/2 Knock-Out Cells by CRISR-Cas9
  - Proliferation and Cell Viability Assays
  - Xenograft Experiment
  - Immunohistochemistry
  - Western Blotting and Antibodies
  - *In Vitro* Cap-Binding Affinity Assay

- Proximity Ligation Assay (PLA)
- Flow Cytometry Analysis of Apoptotic Cells
- Flow Cytometry Analysis of Cytotoxicity
- Measurement of ATP Levels
- Polysome Profiles and RT-qPCR
- Puromycilation Assay
- Glucose Consumption and Lactate Release Assays
- GC/MS and Stable Isotope Tracer Analyses of Cellular Samples
- GC/MS Analyses of Xenograft Tumor Metabolites
- *In Vivo* Infusions of ^{13}C- Labeled Glutamine
- Metabolite Extraction and GC/MS Analysis of Tumor Tissues
- Quantification of Phenformin by LC-MS-MS

- QUANTIFICATION AND STATISTICAL ANALYSIS
- DATA AND SOFTWARE AVAILABILITY

SUPPLEMENTAL INFORMATION

Supplemental Information includes seven figures, two tables, and one data file and can be found with this article online at https://doi.org/10.1016/j.cmet.2018.09.001.

ACKNOWLEDGMENTS

We thank Y. Zhao and E. Birman for technical support; S. McGuirk for the schematics; and LM. Postovit, H. Smith, D. Papadopoli, K. Boulay, and F.A. Mallette for discussion. I.T. (Junior 2) and J.U.-S. (Senior) are supported by FRQ-S. M.M. is supported by the Ministry of Education, Culture, Sports, Science and Technology, Japan (18K07237). M.C. and C. Lehuédé hold the CIHR and FRSQ fellowship, respectively. This work was funded by Canadian Institutes for Health Research (MOP-363027 to I.T., MOP-111143 to J.U.-S., and FDN-148373 to W.M.); NIH to I.T. (R01 CA 202021-01-A1); Terry Fox Research Institute (TFRI-242115) to I.T., M. Pollak, J.S.-P., R.G.J., and P.S.; Canadian Research Chair in Molecular Oncology (950-231033) to W.M.; and Natural Sciences and Engineering Research Council (RGPIN 239108-08) to C.G. The GCRC Metabolomics Core Facility is supported by the Canada Foundation for Innovation, the Dr. John R. and Clara M. Fraser Memorial Trust, the Terry Fox Foundation (TFF Oncometabolism Team Grant 1048 in partnership with the Fondation du Cancer du Sein du Quebec), and McGill University.

AUTHOR CONTRIBUTIONS

Conceptualization, L.H., S.-P.G., M. Pollak, and I.T.; Methodology, L.H., S.-P.G., M.M., M.C., Y.K.I., C. Lehuédé, E.H.M., V.P., T.F., G.B., and D.A.; Formal Analysis, L.H., S.-P.G., M.M., O.L., and C.G.; Investigation, L.H., S.-P.G., M.M., M.C., O.U., Y.K.I., C. Lehuédé, E.H.M., M.L., S.M., M.-J.B., M. Parisotto, V.P., C. Lavoie, G.B., and D.A.; Resources, M.O., T.F., R.G.J., G.F., and W.M.; Writing – Original Draft, L.H., S.-P.G., M. Pollak, and I.T.; Writing – Review & Editing, L.H., S.-P.G., P.S., J.U.-S., J.S.-P., M. Pollak, and I.T.; Funding Acquisition, J.S.-P., M. Pollak, and I.T.; Supervision, J.S.-P., M. Pollak, and I.T.

DECLARATION OF INTERESTS

The authors declare no competing interests.

REFERENCES

Acharya, S., Xu, J., Wang, X., Jain, S., Wang, H., Zhang, Q., Chang, C.C., Bower, J., Arun, B., Seewaldt, V., and Yu, D. (2016). Downregulation of GLUT4 contributes to effective intervention of estrogen receptor-negative/HER2-overexpressing early stage breast disease progression by lapatinib. Am. J. Cancer Res. *6*, 981–995.

Andrzejewski, S., Gravel, S.P., Pollak, M., and St-Pierre, J. (2014). Metformin directly acts on mitochondria to alter cellular bioenergetics. Cancer Metab. *2*, 12.

Balasubramanian, M.N., Butterworth, E.A., and Kilberg, M.S. (2013). Asparagine synthetase: regulation by cell stress and involvement in tumor biology. Am. J. Physiol. Endocrinol. Metab. *304*, E789–E799.

Ben Sahra, I., Laurent, K., Giuliano, S., Larbret, F., Ponzio, G., Gounon, P., Le Marchand-Brustel, Y., Giorgetti-Peraldi, S., Cormont, M., Bertolotto, C., et al. (2010). Targeting cancer cell metabolism: the combination of metformin and 2-deoxyglucose induces p53-dependent apoptosis in prostate cancer cells. Cancer Res. *70*, 2465–2475.

Bhat, M., Robichaud, N., Hulea, L., Sonenberg, N., Pelletier, J., and Topisirovic, I. (2015). Targeting the translation machinery in cancer. Nat. Rev. Drug Discov. *14*, 261–278.

Birsoy, K., Wang, T., Chen, W.W., Freinkman, E., Abu-Remaileh, M., and Sabatini, D.M. (2015). An essential role of the mitochondrial electron transport chain in cell proliferation is to enable aspartate synthesis. Cell *162*, 540–551.

Boudreau, A., Purkey, H.E., Hitz, A., Robarge, K., Peterson, D., Labadie, S., Kwong, M., Hong, R., Gao, M., Del Nagro, C., et al. (2016). Metabolic plasticity underpins innate and acquired resistance to LDHA inhibition. Nat. Chem. Biol. *12*, 779–786.

Brattain, M.G., Fine, W.D., Khaled, F.M., Thompson, J., and Brattain, D.E. (1981). Heterogeneity of malignant cells from a human colonic carcinoma. Cancer Res. *41*, 1751–1756.

Bridges, H.R., Jones, A.J., Pollak, M.N., and Hirst, J. (2014). Effects of metformin and other biguanides on oxidative phosphorylation in mitochondria. Biochem. J. *462*, 475–487.

Brodaczewska, K.K., Szczylik, C., Fiedorowicz, M., Porta, C., and Czarnecka, A.M. (2016). Choosing the right cell line for renal cell cancer research. Mol. Cancer *15*, 83.

Buttgereit, F., and Brand, M.D. (1995). A hierarchy of ATP-consuming processes in mammalian cells. Biochem. J. *312*, 163–167.

Campeau, E., Ruhl, V.E., Rodier, F., Smith, C.L., Rahmberg, B.L., Fuss, J.O., Campisi, J., Yaswen, P., Cooper, P.K., and Kaufman, P.D. (2009). A versatile viral system for expression and depletion of proteins in mammalian cells. PLoS One *4*, e6529.

Chandel, N.S., Avizonis, D., Reczek, C.R., Weinberg, S.E., Menz, S., Neuhaus, R., Christian, S., Haegebarth, A., Algire, C., and Pollak, M. (2016). Are metformin doses used in murine cancer models clinically relevant? Cell Metab. *23*, 569–570.

Clem, B., Telang, S., Clem, A., Yalcin, A., Meier, J., Simmons, A., Rasku, M.A., Arumugam, S., Dean, W.L., Eaton, J., et al. (2008). Small-molecule inhibition of 6-phosphofructo-2-kinase activity suppresses glycolytic flux and tumor growth. Mol. Cancer Ther. *7*, 110–120.

Cummins, E.P., Seeballuck, F., Keely, S.J., Mangan, N.E., Callanan, J.J., Fallon, P.G., and Taylor, C.T. (2008). The hydroxylase inhibitor dimethyloxalylglycine is protective in a murine model of colitis. Gastroenterology *134*, 156–165.

Davidson, S.M., Papagiannakopoulos, T., Olenchock, B.A., Heyman, J.E., Keibler, M.A., Luengo, A., Bauer, M.R., Jha, A.K., O'Brien, J.P., Pierce, K.A., et al. (2016). Environment impacts the metabolic dependencies of Ras-driven non-small cell lung cancer. Cell Metab. *23*, 517–528.

DeBerardinis, R.J., and Chandel, N.S. (2016). Fundamentals of cancer metabolism. Sci. Adv. *2*, e1600200.

DeNicola, G.M., Chen, P.H., Mullarky, E., Sudderth, J.A., Hu, Z., Wu, D., Tang, H., Xie, Y., Asara, J.M., Huffman, K.E., et al. (2015). NRF2 regulates serine biosynthesis in non-small cell lung cancer. Nat. Genet. *47*, 1475–1481.

Dodd, K.M., Yang, J., Shen, M.H., Sampson, J.R., and Tee, A.R. (2015). mTORC1 drives HIF-1α and VEGF-A signalling via multiple mechanisms involving 4E-BP1, S6K1 and STAT3. Oncogene *34*, 2239–2250.

Dowling, R.J., Topisirovic, I., Alain, T., Bidinosti, M., Fonseca, B.D., Petroulakis, E., Wang, X., Larsson, O., Selvaraj, A., Liu, Y., et al. (2010). mTORC1-mediated cell proliferation, but not cell growth, controlled by the 4E-BPs. Science *328*, 1172–1176.

Dowling, R.J., Lam, S., Bassi, C., Mouaaz, S., Aman, A., Kiyota, T., Al-Awar, R., Goodwin, P.J., and Stambolic, V. (2016). Metformin pharmacokinetics in mouse tumors: implications for human therapy. Cell Metab. *23*, 567–568.

Gameiro, P.A., Yang, J., Metelo, A.M., Pérez-Carro, R., Baker, R., Wang, Z., Arreola, A., Rathmell, W.K., Olumi, A., López-Larrubia, P., et al. (2013). In vivo HIF-mediated reductive carboxylation is regulated by citrate levels and sensitizes VHL-deficient cells to glutamine deprivation. Cell Metab. *17*, 372–385.

Gandin, V., Sikström, K., Alain, T., Morita, M., McLaughlan, S., Larsson, O., and Topisirovic, I. (2014). Polysome fractionation and analysis of mammalian translatomes on a genome-wide scale. J. Vis. Exp. https://doi.org/10.3791/51455.

Gandin, V., Masvidal, L., Cargnello, M., Gyenis, L., McLaughlan, S., Cai, Y., Tenkerian, C., Morita, M., Balanathan, P., Jean-Jean, O., et al. (2016a). mTORC1 and CK2 coordinate ternary and eIF4F complex assembly. Nat. Commun. *7*, 11127.

Gandin, V., Masvidal, L., Hulea, L., Gravel, S.P., Cargnello, M., McLaughlan, S., Cai, Y., Balanathan, P., Morita, M., Rajakumar, A., et al. (2016b). nanoCAGE reveals 5′ UTR features that define specific modes of translation of functionally related MTOR-sensitive mRNAs. Genome Res. *26*, 636–648.

Geyer, C.E., Forster, J., Lindquist, D., Chan, S., Romieu, C.G., Pienkowski, T., Jagiello-Gruszfeld, A., Crown, J., Chan, A., Kaufman, B., et al. (2006). Lapatinib plus capecitabine for HER2-positive advanced breast cancer. N. Engl. J. Med. *355*, 2733–2743.

Giard, D.J., Aaronson, S.A., Todaro, G.J., Arnstein, P., Kersey, J.H., Dosik, H., and Parks, W.P. (1973). In vitro cultivation of human tumors: establishment of cell lines derived from a series of solid tumors. J. Natl. Cancer Inst. *51*, 1417–1423.

Gravel, S.P., Hulea, L., Toban, N., Birman, E., Blouin, M.J., Zakikhani, M., Zhao, Y., Topisirovic, I., St-Pierre, J., and Pollak, M. (2014). Serine deprivation enhances antineoplastic activity of biguanides. Cancer Res. *74*, 7521–7533.

Gravel, S.P., Avizonis, D., and St-Pierre, J. (2016). Metabolomics analyses of cancer cells in controlled microenvironments. Methods Mol. Biol. *1458*, 273–290.

Gwinn, D.M., Lee, A.G., Briones-Martin-Del-Campo, M., Conn, C.S., Simpson, D.R., Scott, A.I., Le, A., Cowan, T.M., Ruggero, D., and Sweet-Cordero, E.A. (2018). Oncogenic KRAS regulates amino acid homeostasis and asparagine biosynthesis via ATF4 and alters sensitivity to L-asparaginase. Cancer Cell *33*, 91–107.e6.

Heir, P., Srikumar, T., Bikopoulos, G., Bunda, S., Poon, B.P., Lee, J.E., Raught, B., and Ohh, M. (2016). Oxygen-dependent regulation of erythropoietin receptor turnover and signaling. J. Biol. Chem. *291*, 7357–7372.

Hettmer, S., Schinzel, A.C., Tchessalova, D., Schneider, M., Parker, C.L., Bronson, R.T., Richards, N.G., Hahn, W.C., and Wagers, A.J. (2015). Functional genomic screening reveals asparagine dependence as a metabolic vulnerability in sarcoma. Elife *4*, https://doi.org/10.7554/eLife.09436.

Hill, J.M., Roberts, J., Loeb, E., Khan, A., MacLellan, A., and Hill, R.W. (1967). L-asparaginase therapy for leukemia and other malignant neoplasms. Remission in human leukemia. JAMA *202*, 882–888.

Javeshghani, S., Zakikhani, M., Austin, S., Bazile, M., Blouin, M.J., Topisirovic, I., St-Pierre, J., and Pollak, M.N. (2012). Carbon source and myc expression influence the antiproliferative actions of metformin. Cancer Res. *72*, 6257–6267.

Jiang, L., Shestov, A.A., Swain, P., Yang, C., Parker, S.J., Wang, Q.A., Terada, L.S., Adams, N.D., McCabe, M.T., Pietrak, B., et al. (2016). Reductive carboxylation supports redox homeostasis during anchorage-independent growth. Nature *532*, 255–258.

Knott, S.R.V., Wagenblast, E., Khan, S., Kim, S.Y., Soto, M., Wagner, M., Turgeon, M.O., Fish, L., Erard, N., Gable, A.L., et al. (2018). Asparagine bioavailability governs metastasis in a model of breast cancer. Nature *554*, 378–381.

Kordes, S., Pollak, M.N., Zwinderman, A.H., Mathôt, R.A., Weterman, M.J., Beeker, A., Punt, C.J., Richel, D.J., and Wilmink, J.W. (2015). Metformin in patients with advanced pancreatic cancer: a double-blind, randomised, placebo-controlled phase 2 trial. Lancet Oncol. *16*, 839–847.

Krstic, J., Trivanovic, D., Jaukovic, A., Santibanez, J.F., and Bugarski, D. (2017). Metabolic plasticity of stem cells and macrophages in cancer. Front. Immunol. *8*, 939.

Larsson, O., Morita, M., Topisirovic, I., Alain, T., Blouin, M.J., Pollak, M., and Sonenberg, N. (2012). Distinct perturbation of the translatome by the antidiabetic drug metformin. Proc. Natl. Acad. Sci. USA *109*, 8977–8982.

Le, X.F., Mao, W., Lu, C., Thornton, A., Heymach, J.V., Sood, A.K., and Bast, R.C., Jr. (2008). Specific blockade of VEGF and HER2 pathways results in greater growth inhibition of breast cancer xenografts that overexpress HER2. Cell Cycle *7*, 3747–3758.

Lehuédé, C., Dupuy, F., Rabinovitch, R., Jones, R.G., and Siegel, P.M. (2016). Metabolic plasticity as a determinant of tumor growth and metastasis. Cancer Res. *76*, 5201–5208.

Leprivier, G., Remke, M., Rotblat, B., Dubuc, A., Mateo, A.R., Kool, M., Agnihotri, S., El-Naggar, A., Yu, B., Somasekharan, S.P., et al. (2013). The eEF2 kinase confers resistance to nutrient deprivation by blocking translation elongation. Cell *153*, 1064–1079.

Ling, A.M., and Keech, D.B. (1966). Pyruvate carboxylase from sheep kidney. I. Purification and some properties of the enzyme. Enzymologia *30*, 367–380.

Liu, J., Pan, C., Guo, L., Wu, M., Guo, J., Peng, S., Wu, Q., and Zuo, Q. (2016). A new mechanism of trastuzumab resistance in gastric cancer: MACC1 promotes the Warburg effect via activation of the PI3K/AKT signaling pathway. J. Hematol. Oncol. *9*, 76.

Lozzio, C.B., and Lozzio, B.B. (1975). Human chronic myelogenous leukemia cell-line with positive Philadelphia chromosome. Blood *45*, 321–334.

Mali, P., Yang, L., Esvelt, K.M., Aach, J., Guell, M., DiCarlo, J.E., Norville, J.E., and Church, G.M. (2013). RNA-guided human genome engineering via Cas9. Science *339*, 823–826.

Mattaini, K.R., Sullivan, M.R., and Vander Heiden, M.G. (2016). The importance of serine metabolism in cancer. J. Cell Biol. *214*, 249–257.

Maxwell, P.H., Wiesener, M.S., Chang, G.W., Clifford, S.C., Vaux, E.C., Cockman, M.E., Wykoff, C.C., Pugh, C.W., Maher, E.R., and Ratcliffe, P.J. (1999). The tumour suppressor protein VHL targets hypoxia-inducible factors for oxygen-dependent proteolysis. Nature *399*, 271–275.

McArthur, G.A., Puzanov, I., Amaravadi, R., Ribas, A., Chapman, P., Kim, K.B., Sosman, J.A., Lee, R.J., Nolop, K., Flaherty, K.T., et al. (2012). Marked, homogeneous, and early [18F]fluorodeoxyglucose-positron emission tomography responses to vemurafenib in BRAF-mutant advanced melanoma. J. Clin. Oncol. *30*, 1628–1634.

Miloslavski, R., Cohen, E., Avraham, A., Iluz, Y., Hayouka, Z., Kasir, J., Mudhasani, R., Jones, S.N., Cybulski, N., Rüegg, M.A., et al. (2014). Oxygen sufficiency controls TOP mRNA translation via the TSC-Rheb-mTOR pathway in a 4E-BP-independent manner. J. Mol. Cell Biol. *6*, 255–266.

Molina, J.R., Sun, Y., Protopopova, M., Gera, S., Bandi, M., Bristow, C., McAfoos, T., Morlacchi, P., Ackroyd, J., Agip, A.A., et al. (2018). An inhibitor of oxidative phosphorylation exploits cancer vulnerability. Nat. Med. *24*, 1036–1046.

Morita, M., Gravel, S.P., Chénard, V., Sikström, K., Zheng, L., Alain, T., Gandin, V., Avizonis, D., Arguello, M., Zakaria, C., et al. (2013). mTORC1 controls mitochondrial activity and biogenesis through 4E-BP-dependent translational regulation. Cell Metab. *18*, 698–711.

Mullen, A.R., Wheaton, W.W., Jin, E.S., Chen, P.H., Sullivan, L.B., Cheng, T., Yang, Y., Linehan, W.M., Chandel, N.S., and DeBerardinis, R.J. (2011). Reductive carboxylation supports growth in tumour cells with defective mitochondria. Nature *481*, 385–388.

Munday, M.R. (2002). Regulation of mammalian acetyl-CoA carboxylase. Biochem. Soc. Trans. *30*, 1059–1064.

Phannasil, P., Ansari, I.H., El Azzouny, M., Longacre, M.J., Rattanapornsompong, K., Burant, C.F., MacDonald, M.J., and Jitrapakdee, S. (2017). Mass spectrometry analysis shows the biosynthetic pathways supported by pyruvate carboxylase in highly invasive breast cancer cells. Biochim. Biophys. Acta *1863*, 537–551.

Poliaková, M., Aebersold, D.M., Zimmer, Y., and Medová, M. (2018). The relevance of tyrosine kinase inhibitors for global metabolic pathways in cancer. Mol. Cancer *17*, 27.

Pollak, M. (2013). Targeting oxidative phosphorylation: why, when, and how. Cancer Cell *23*, 263–264.

Poon, I.K., Lucas, C.D., Rossi, A.G., and Ravichandran, K.S. (2014). Apoptotic cell clearance: basic biology and therapeutic potential. Nat. Rev. Immunol. *14*, 166–180.

Ravaud, A., Hawkins, R., Gardner, J.P., von der Maase, H., Zantl, N., Harper, P., Rolland, F., Audhuy, B., Machiels, J.P., Pétavy, F., et al. (2008). Lapatinib versus hormone therapy in patients with advanced renal cell carcinoma: a randomized phase III clinical trial. J. Clin. Oncol. *26*, 2285–2291.

Ron, D., and Harding, H.P. (2007). eIF2α phosphorylation in cellular stress-responses and disease. In Translational Control in Biology and Medicine, M.B. Mathews, N. Sonenberg, and J.W.B. Hershey, eds. (Cold Spring Harbor Laboratory Press), pp. 345–368.

Schito, L., and Rey, S. (2017). Hypoxic pathobiology of breast cancer metastasis. Biochim. Biophys. Acta *1868*, 239–245.

Sellers, K., Fox, M.P., Bousamra, M., 2nd, Slone, S.P., Higashi, R.M., Miller, D.M., Wang, Y., Yan, J., Yuneva, M.O., Deshpande, R., et al. (2015). Pyruvate carboxylase is critical for non-small-cell lung cancer proliferation. J. Clin. Invest. *125*, 687–698.

Selvarajah, J., Nathawat, K., Moumen, A., Ashcroft, M., and Carroll, V.A. (2013). Chemotherapy-mediated p53-dependent DNA damage response in clear cell renal cell carcinoma: role of the mTORC1/2 and hypoxia-inducible factor pathways. Cell Death Dis. *4*, e865.

Semenza, G.L. (2007). Hypoxia-inducible factor 1 (HIF-1) pathway. Sci. STKE *2007*, cm8.

Semenza, G.L. (2013). HIF-1 mediates metabolic responses to intratumoral hypoxia and oncogenic mutations. J. Clin. Invest. *123*, 3664–3671.

Snell, K. (1984). Enzymes of serine metabolism in normal, developing and neoplastic rat tissues. Adv. Enzyme Regul. *22*, 325–400.

Sun, R.C., and Denko, N.C. (2014). Hypoxic regulation of glutamine metabolism through HIF1 and SIAH2 supports lipid synthesis that is necessary for tumor growth. Cell Metab. *19*, 285–292.

Tallarida, R.J. (2006). An overview of drug combination analysis with isobolograms. J. Pharmacol. Exp. Ther. *319*, 1–7.

Trousil, S., Chen, S., Mu, C., Shaw, F.M., Yao, Z., Ran, Y., Shakuntala, T., Merghoub, T., Manstein, D., Rosen, N., et al. (2017). Phenformin enhances the efficacy of ERK inhibition in NF1-mutant melanoma. J. Invest. Dermatol. *137*, 1135–1143.

Ursini-Siegel, J., Rajput, A.B., Lu, H., Sanguin-Gendreau, V., Zuo, D., Papavasiliou, V., Lavoie, C., Turpin, J., Cianflone, K., Huntsman, D.G., and Muller, W.J. (2007). Elevated expression of DecR1 impairs ErbB2/Neu-induced mammary tumor development. Mol. Cell. Biol. *27*, 6361–6371.

Ursini-Siegel, J., Hardy, W.R., Zuo, D., Lam, S.H., Sanguin-Gendreau, V., Cardiff, R.D., Pawson, T., and Muller, W.J. (2008). ShcA signalling is essential for tumour progression in mouse models of human breast cancer. EMBO J. *27*, 910–920.

Vander Heiden, M.G., and DeBerardinis, R.J. (2017). Understanding the intersections between metabolism and cancer biology. Cell *168*, 657–669.

Vazquez-Martin, A., Oliveras-Ferraros, C., Del Barco, S., Martin-Castillo, B., and Menendez, J.A. (2011). The anti-diabetic drug metformin suppresses self-renewal and proliferation of trastuzumab-resistant tumor-initiating breast cancer stem cells. Breast Cancer Res. Treat. *126*, 355–364.

Wheaton, W.W., Weinberg, S.E., Hamanaka, R.B., Soberanes, S., Sullivan, L.B., Anso, E., Glasauer, A., Dufour, E., Mutlu, G.M., Budigner, G.S., and Chandel, N.S. (2014). Metformin inhibits mitochondrial complex I of cancer cells to reduce tumorigenesis. Elife *3*, e02242.

Whelan, K.A., Schwab, L.P., Karakashev, S.V., Franchetti, L., Johannes, G.J., Seagroves, T.N., and Reginato, M.J. (2013). The oncogene HER2/neu (ERBB2) requires the hypoxia-inducible factor HIF-1 for mammary tumor growth and anoikis resistance. J. Biol. Chem. *288*, 15865–15877.

Yuan, P., Ito, K., Perez-Lorenzo, R., Del Guzzo, C., Lee, J.H., Shen, C.H., Bosenberg, M.W., McMahon, M., Cantley, L.C., and Zheng, B. (2013). Phenformin enhances the therapeutic benefit of BRAF(V600E) inhibition in melanoma. Proc. Natl. Acad. Sci. USA *110*, 18226–18231.

Zhang, J., Fan, J., Venneti, S., Cross, J.R., Takagi, T., Bhinder, B., Djaballah, H., Kanai, M., Cheng, E.H., Judkins, A.R., et al. (2014). Asparagine plays a critical role in regulating cellular adaptation to glutamine depletion. Mol. Cell *56*, 205–218.

Zhang, L., Han, J., Jackson, A.L., Clark, L.N., Kilgore, J., Guo, H., Livingston, N., Batchelor, K., Yin, Y., Gilliam, T.P., et al. (2016). NT1014, a novel biguanide, inhibits ovarian cancer growth in vitro and in vivo. J. Hematol. Oncol. *9*, 91.

Zhang, B., Zheng, A., Hydbring, P., Ambroise, G., Ouchida, A.T., Goiny, M., Vakifahmetoglu-Norberg, H., and Norberg, E. (2017). PHGDH defines a metabolic subtype in lung adenocarcinomas with poor prognosis. Cell Rep. *19*, 2289–2303.

Zhdanov, A.V., Okkelman, I.A., Collins, F.W., Melgar, S., and Papkovsky, D.B. (2015). A novel effect of DMOG on cell metabolism: direct inhibition of mitochondrial function precedes HIF target gene expression. Biochim. Biophys. Acta *1847*, 1254–1266.

STAR★METHODS

KEY RESOURCES TABLE

REAGENT or RESOURCE	SOURCE	IDENTIFIER
Antibodies		
Mouse monoclonal β-actin antibody	Sigma-Aldrich	A5441; RRID: AB_476744
Rabbit monoclonal phospho-4E-BP1 (S65) (174A9) antibody	Cell Signaling Technology	9456; RRID: AB_823413
Rabbit monoclonal 4E-BP1 (53H11) antibody	Cell Signaling Technology	9644; RRID: AB_2097841
Rabbit polyclonal 4E-BP2 antibody	Cell Signaling Technology	2845; RRID: AB_10699019
Rabbit monoclonal phospho-S6K (T389) antibody	Cell Signaling Technology	9234; RRID: AB_2269803
Rabbit monoclonal S6K1 antibody	Cell Signaling Technology	2708; RRID: AB_390722
Rabbit polyclonal phospho-S6 Ribosomal Protein (Ser240/244) antibody	Cell Signaling Technology	2215; RRID: AB_2630325
Mouse monoclonal S6 ribosomal protein antibody	Santa Cruz Biotechnology	sc-74459; RRID: AB_1129205
Rabbit polyclonal ACC antibody	Cell Signaling Technology	3662; RRID: AB_2219400
Rabbit polyclonal phosphor-ACC (Ser79) antibody	Cell Signaling Technology	3661; RRID: AB_330337
Rabbit polyclonal ERK1/2 antibody	Cell Signaling Technology	9102; RRID: AB_330744
Rabbit polyclonal phospho-ERK1/2 (Thr202/Tyr204) antibody	Cell Signaling Technology	9101; RRID: AB_331646
Mouse monoclonal eIF2α (L57A5) antibody	Cell Signaling Technology	2103; RRID: AB_836874
Rabbit polyclonal eIF2α (Ser51) antibody	Cell Signaling Technology	9721; RRID: AB_330951
Rabbit monoclonal c-Myc (D84C12) antibody	Cell Signaling Technology	9402; RRID: AB_2151827
Mouse monoclonal anti-Cyclin D3 (DCS22) antibody	Cell Signaling Technology	2936; RRID: AB_2070801
Rabbit polyclonal eIF4G1 antibody	Cell Signaling Technology	2858; RRID: AB_2095745
Mouse monoclonal BCL-2 (50E3) antibody	Cell Signaling Technology	2870; RRID: AB_2290370
Rabbit polyclonal TFAM antibody	Cell Signaling Technology	7495; RRID: AB_10841294
Rabbit monoclonal GAPDH (14C10) antibody	Cell Signaling Technology	2118; RRID: AB_561053
Mouse monoclonal eIF4E antibody	BD Biosciences	610269; RRID: AB_397664
Rabbit polyclonal MCL-1 (H-260) antibody	Santa Cruz Biotechnology	sc-20679; RRID: AB_2144111
Rabbit polyclonal pyruvate carboxylase (PCB; H-300) antibody	Santa Cruz Biotechnology	67021; RRID: AB_2283532
Rabbit polyclonal survivin antibody	Abcam	ab175809
Rabbit polyclonal ASNS antibody	Novus Biologicals	NBP1-87444; RRID: AB_11036043
Rabbit polyclonal PSAT antibody	Novus Biologicals	NBP1-32920; RRID: AB_2172600
Rabbit polyclonal HIF-2α antibody	Novus Biologicals	NB100-122; RRID: AB_350059
Rabbit polyclonal HIF-1α antibody	Cayman Chemical	10006421; RRID: AB_409037
Rabbit polyclonal OGDH antibody	Abcam	ab87057; RRID: AB_2156766
Rabbit polyclonal GOT1 antibody	Abcam	ab189863
Rabbit polyclonal TFAM antibody	Abcam	ab131607; RRID: AB_11154693
Mouse monoclonal puromycin (12D10) antibody	Millipore	MABE343; RRID: AB_2566826
Rabbit polyclonal HA antibody	Sigma-Aldrich	H6908; RRID: AB_260070
Rabbit polyclonal PHGDH antibody	Sigma-Aldrich	HPA021241; RRID: AB_1855399
Chemicals, Peptides, and Recombinant Proteins		
torin1	Tocris Bioscience	4247
lapatinib ditosylate	Selleckchem	S1028
PLX4032	Selleckchem	S1267
imatinib mesylate	Selleckchem	S1026
phenformin hydrochloride	Sigma-Aldrich	P7045
dimethyloxallyl glycine (DMOG)	Sigma-Aldrich	D3695
3PO	Calbiochem	525330
L-aspartic acid	Sigma-Aldrich	A9256

(*Continued on next page*)

Continued

REAGENT or RESOURCE	SOURCE	IDENTIFIER
L-asparagine	Sigma-Aldrich	A0884
L-asparaginase	Montreal Jewish General Hospital pharmacy	N/A
hexadimethrine bromide (polybrene)	Sigma-Aldrich	107689
puromycin, dihydrochloride	Bio Basic	PJ593
hygromycin B	Wisent	450-141-XL
G418 sulfate	Bio Basic	GDJ958
lipofectamine 2000	Thermo Fisher Scientific	11668027
tween-80	Sigma-Aldrich	P4780
methyl cellulose	Sigma-Aldrich	274429
Critical Commercial Assays		
Cell Proliferation Elisa BrdU (colorimetric)	Roche	11647229001
Pierce BCA Protein Assay Kit	Thermo Fisher Scientific	23225
Duolink *In situ* red mouse/rabbit kit	Sigma-Aldrich	DUO92101
FITC Annexin V Apoptosis Detection Kit	BD Biosciences	556547
Luminescent ATP Detection Assay Kit	Abcam	ab113849
Deposited Data		
Raw and analyzed data	This paper	https://doi.org/10.17632/4k6knxb996.2
Experimental Models: Cell Lines		
A375 cells	ATCC	CRL-1619
NMuMG	(Ursini-Siegel et al., 2008)	N/A
NT2197	(Ursini-Siegel et al., 2008)	N/A
K562	ATCC	CCI-243
HCT116	(Gandin et al., 2016a)	N/A
RCC4 mock and RCC4-VHL	(Selvarajah et al., 2013)	N/A
IMR90	Coriell Institute for Medical Research	I90-10
WT ($p53^{-/-}$) MEFs	(Dowling et al., 2010)	N/A
Oligonucleotides		
qPCR primer: mCyclinD3Fw: CGAGCCTCCTACTTCCAGTG	(Dowling et al., 2010)	N/A
qPCR primer: mCyclinD3Rv: GGACAGGTAGCGATCCAGGT	(Dowling et al., 2010)	N/A
qPCR primer: mGAPDH Fw: TGTGTCCGTCGTGGATCTGAC	This paper	N/A
qPCR primer: mGAPDH Rv: CACCCTGTTGCTGTAGCCGTA	This paper	N/A
qPCR primer: mBACTIN Fw: TTCCTTCTTGGGTATGGAA	This paper	N/A
qPCR primer: mBACTIN Rv: CCACGATCCACACAGAGTA	This paper	N/A
qPCR primer: mASNSFw: CTGTTTGATGTTCTCCGGGC	This paper	N/A
qPCR primer: mASNSRv: GGTAGCAGGTTGCAGTCCTC	This paper	N/A
qPCR primer: mPHGDHfor: CTGATGCACGCCTGGGCTGG	This paper	N/A
qPCR primer: mPHGDHrev: CCTGCTCCCCTGGAACCCCA	This paper	N/A
A complete list of oligonucleotides used in this study is provided in Table S2.	N/A	N/A
Recombinant DNA		
pLKO.1 Non-Target shRNA Control	Sigma-Aldrich	SHC002
pLKO.1 hHIF-1α shRNA	Sigma-Aldrich	TRCN0000003810
pLKO.1 hIDH1 shRNA	Sigma-Aldrich	TRCN0000027298
a pLKO.1-neo vector control	a gift from Sheila Stewart	Addgene 13425
pLKO.1-neo-mIDH1 shRNA	This paper	N/A
pLV-Hygro-U6 mPHGDH shRNA	This paper	N/A
pLV-Hygro-U6 mASNS shRNA	This paper	N/A

(*Continued on next page*)

Continued

REAGENT or RESOURCE	SOURCE	IDENTIFIER
hCas9	(Mali et al., 2013)	Addgene 41815
CRISPR gRNA h4E-BP1	GeneCopoeia	HCP204676-SG01-3-B-a
CRISPR gRNA h4E-BP1	GeneCopoeia	HCP204676-SG01-3-B-b
CRISPR gRNA h4E-BP1	GeneCopoeia	HCP204676-SG01-3-B-c
CRISPR gRNA h4E-BP2	GeneCopoeia	HCP254214-SG01-3-B-a
CRISPR gRNA h4E-BP2	GeneCopoeia	HCP254214-SG01-3-B-b
CRISPR gRNA h4E-BP2	GeneCopoeia	HCP254214-SG01-3-B-c
CRISPR gRNA m4E-BP1	GeneCopoeia	MCP227000-SG01-3-B-a
CRISPR gRNA m4E-BP1	GeneCopoeia	MCP227000-SG01-3-B-b
CRISPR gRNA m4E-BP1	GeneCopoeia	MCP227000-SG01-3-B-c
CRISPR gRNA m4E-BP2	GeneCopoeia	MCP229088-SG01-3-B-a
CRISPR gRNA m4E-BP2	GeneCopoeia	MCP229088-SG01-3-B-b
CRISPR gRNA m4E-BP2	GeneCopoeia	MCP229088-SG01-3-B-c
pBabe-puro	(Dowling et al., 2010)	N/A
pQCXIB (blast)	(Campeau et al., 2009)	Addgene 17487
pLV-Neo-CMV-4E-BP1	This study	N/A
Software and Algorithms		
R	The R Project for Statistical Computing	N/A
ImageJ	NCBI	https://imagej.nih.gov/ij/index.html
Chemstation	Agilent	N/A
MassHunter	Agilent	N/A
Aperio Imagescope	Leica Biosystems	N/A
FlowJo	FlowJo, LLC	N/A
FacsDiva	BD Biosciences	N/A
GraphPad Prism 7.0	GraphPad Software	https://www.graphpad.com/

CONTACT FOR REAGENT AND RESOURCE SHARING

Further information and requests for reagents should be directed to and will be fulfilled by the Lead Contact, Ivan Topisirovic (ivan.topisirovic@mcgill.ca).

EXPERIMENTAL MODEL AND SUBJECT DETAILS

Cell Lines and Cell Culture Conditions

NMuMG and NMuMG-NT2197 cells were cultured in Dulbecco's modified Eagle's medium (DMEM; Wisent #319-005-CL), supplemented with 10% heat-inactivated fetal bovine serum (Wisent), 1% penicillin/streptomycin (Wisent; #450-201-EL) and 2mM L-Glutamine (Wisent, #609-065-EL) to obtain 6mM L-Glutamine final concentration, 10 μg/mL insulin, 20 mM HEPES, pH 7.5 (Wisent, #330-050-EL), as previously described (Ursini-Siegel et al., 2008). For NT2197 cells, puromycin (2 μg/mL) was added to the media. A375 cells were obtained from ATCC (#CRL-1619). IMR90 cells were obtained from the Coriell Institute for Medical Research. A375, IMR90, HCT116 (Gandin et al., 2016a) and MEF (Dowling et al., 2010) cells were maintained in DMEM supplemented with 10% fetal bovine serum (Wisent), 1% penicillin/streptomycin (Wisent; #450-201-EL) and 2mM L-Glutamine (Wisent, #609-065-EL) to obtain 6mM L-Glutamine final concentration. K562 cells were obtained from ATCC (#CCL-243) and were cultured in RPMI-1640 (Wisent), supplemented with 10% fetal bovine serum (Wisent) and 1% penicillin/streptomycin (Wisent; #450-201-EL). RCC4 mock or expressing VHL-HA (Selvarajah et al., 2013) were cultured in DMEM supplemented with 10% fetal bovine serum (Wisent), 1% penicillin/streptomycin (Wisent; #450-201-EL) and 250 μg/mL G418. Lack of mycoplasma contamination was confirmed using Mycoplasma PCR Detection Kit (Applied Biological Materials). HCT116, K562 and A375 were verified using ATCC Cell line authentication service [profiling of 17 short tandem repeats (STR) and 1 gender determination locus]. The results were: (i) for HCT116, 94% match to ATCC HCT116 # CCL-247 [D5S818 (10, 11 versus 10, 11); D13S317 (10, 12 versus 10, 12); D7S820 (11, 12 versus 11, 12); D16S539 (11, 12, 13, 14 versus 11, 13); vWA (17, 21, 22, 23 versus 17, 22); THO1 (8, 9 versus 8,9); AMEL (X versus XY); TPOX (8, 9 versus 8, 9), CSF1PO (7, 10 versus 7, 10)]; (ii) for K562, 100% match to ATCC K562 # CCL-243 [D5S818 (11, 12 versus 11, 12); D13S317 (8 versus 8); D7S820 (9, 11 versus 9, 11); D16S539 (11, 12 versus 11, 12); vWA (16 versus 16); THO1 (9.3 versus 9.3);

AMEL (X versus X); TPOX (8, 9 versus 8, 9), CSF1PO (9, 10 versus 9, 10)]; (iii) for A375, 100% match to ATCC A375 # CRL-1619 [D5S818 (12 versus 12); D13S317 (11, 14 versus 11, 14); D7S820 (9 versus 9); D16S539 (9 versus 9); vWA (16, 17 versus 16, 17); THO1 (8 versus 8); AMEL (X versus X); TPOX (8, 10 versus 8, 10), CSF1PO (11, 12 versus 11, 12)].

Where indicated, cells were treated with lapatinib ditosylate (Selleckchem), PLX4032 (Selleckchem), imatinib mesylate (Selleckchem), phenformin hydrochloride (Sigma), torin1 (Tocris Bioscience), 3-PO (Calbiochem), dimethyloxallyl glycine (DMOG; Sigma), L-aspartic acid (Sigma), L-asparagine (Sigma), or L-asparaginase (SMBD JGH pharmacy; 5000units/mL stock).

METHOD DETAILS

Generation of Knock-Down Cell Lines by shRNA

Puromycin resistant pLKO.1 lentiviral shRNA vectors were retrieved from the arrayed Mission TRC genome-wide shRNA collections purchased from Sigma-Aldrich Corporation. Additional information about the shRNA vectors can be found at https://www.sigmaaldrich.com/life-science/functional-genomics-and-rnai/shrna/individual-genes.html or https://www.broadinstitute.org/rnai-consortium/rnai-consortium-shrna-library, using the TRCN number. The following lentiviral shRNA vector were used: TRCN0000003810 (hHIF-1α) and TRCN0000027298 (hIDH1). The Non-Target shRNA Control (Sigma: SHC002) was used as negative control. shRNA sequences from TRCN0000041627 (mPHGDH) and TRCN0000324779 (mASNS) were subcloned into pLV[shRNA]-Hygro-U6 (by VectorBuilder), and that from TRCN0000041715 (mIDH1) into a pLKO.1-neo vector (a gift from Sheila Stewart, Addgene 13425), to change antibiotic selection. Lentiviral supernatants were generated as described at https://portals.broadinstitute.org/gpp/public/resources/protocols. Supernatants were applied on target cells with polybrene (6 μg/mL). Cells were reinfected the next day and, 2 days later, selected with puromycin (4 μg/mL; Bio Basic), hygromycin B (400 μg/mL, Wisent) or G418 (250 μg/mL, Bio Basic) for 72 hours.

Generation of 4E-BP1/2 Knock-Out Cells by CRISR-Cas9

A375 cells were transfected in 6-well plates with a plasmid expressing hCas9 [0.7 μg; a gift from George Church (Addgene plasmid # 41815) (Mali et al., 2013)]; three guides RNAs (gRNAs) targeting h4E-BP1 (purchased from GeneCopoeia, cat. # HCP204676-SG01-3-B-a; HCP204676-SG01-3-B-b; and HCP204676-SG01-3-B-c against h4E-BP1 sequences CCGCCCGCCCGCTTATCTTC; GTGAGTTCCGACACTCCATC; and TGAAGAGTCACAGTTTGAGA, respectively); three gRNAs targeting h4E-BP2 (purchased from GeneCopoeia, cat. # HCP254214-SG01-3-B-a; HCP254214-SG01-3-B-b; and HCP254214-SG01-3-B-c against h4E-BP2 sequences GTGGCCGCTGCCGGCTGACG; CTAGTGACTCCTGGGATATT; and ACAACTTGAACAATCACGAC, respectively) (0.2 μg for each gRNA to total 1.2 μg); and pBabe-puro (0.6 μg), using Lipofectamine 2000 (Invitrogen), according to the manufacturers instruction. As a control, cells were transfected with plasmids expressing hCas9 (0.7 μg) and pBabe-puro (0.6 μg), using Lipofectamine 2000 (Invitrogen). NT2197 cells were transfected in 6-well plates with a plasmid expressing hCas9 (0.7 μg); three gRNAs targeting m4E-BP1 (purchased from GeneCopoeia, cat. # MCP227000-SG01-3-B-a; MCP227000-SG01-3-B-b; and MCP227000-SG01-3-B-c against m4E-BP1 sequences GAGCTGCACGCCATCGCCGA; CGTGCAGGAGACATGTCGGC; and GACTACAGCACCA CTCCGGG, respectively); three gRNAs targeting m4E-BP2 (purchased from GeneCopoeia, cat. # MCP229088-SG01-3-B-a; MCP229088-SG01-3-B-b; and MCP229088-SG01-3-B-c against m4E-BP2 sequences GGAGCCATGTCCGCGTCGGC; CTGATA GCCACGGTGCGCGT; and GCGCCATGGGAGAATTGCGA, respectively) (0.2 μg for each gRNA to total 1.2 μg); and pQCXIB(blast) (0.6 μg), using Lipofectamine 2000 (Invitrogen), according to the manufacturers instruction. As a control, cells were transfected with plasmids expressing hCas9 (0.7 μg) and pQCXIB(blast) (0.6 μg), using Lipofectamine 2000 (Invitrogen). Two days post-transfection, A375 cells were selected for 3 days with puromycin (4 μg/mL) and NT2197 were selected for 3 days with blasticidin (8 μg/mL), to remove non-transfected cells. Following selection, NT2197 and A375 cells were seeded in 96-well plates at a density of single cell/well in puromycin or blasticidin free media. Cells were monitored for the presence of single colonies/well. Single cell colonies were amplified to generate cell lines and the expression of 4E-BP1 and 4E-BP2 was analyzed by western blot. Lines with loss of 4E-BP1 and 4E-BP2 expression were kept for further experiments. For the control cells, single cell colonies were amplified and 5 of the control lines were pooled to generate the A375 or NT2197 CRISPR control population. NT2197 4E-BP DKO cl17 cells re-expressing 4E-BP1 were generating using pLV-Neo-CMV-4E-BP1 and selected with 250 μg/mL G418.

Proliferation and Cell Viability Assays

For the bromodeoxyuridine (BrdU) incorporation assay (Cell Proliferation ELISA BrdU Kit from Roche), cells were seeded in 96-well plates (1000 cells/well for all cell lines except 5000 cells/well for IMR90) and maintained as indicated in the figure legends of Figures 1, 2, 4, 6, 7, S1–S4, S6, and S7 for 72h. Tests were performed in triplicate, with each microplate including media and DMSO control wells, as per the manufacturer's instruction. Absorbance at 370nm (reference wavelength 492nm) was measured using a Benchmark Plus microplate reader (Bio-Rad). Combination index$_{50}$ (CI$_{50}$) was calculated using the isobologram equation (CI$_{50}$) = (a/A) + (b/B), where, A and B represent the IC$_{50}$ concentrations of KI (lapatinib, PLX4232 or imatinib) and phenformin when administered alone, a and b represent the concentrations required for the same effect when KI and phenformin were administered in combination, and CI$_{50}$ represents an index of drug interaction (combination index). CI$_{50}$ values of < 1 indicate synergy, a CI$_{50}$ value of 1 represents additivity, and CI$_{50}$ values of > 1 indicate antagonism (Tallarida, 2006). Data points shown are representative of 2-3 independent experiments (n = 3 technical replicates). Viable cell count was performed as previously described (Gravel et al., 2014). Briefly, cells were seeded in 6-well culture plates, treated 24h later as indicated in figure legends of Figures S1, S2, S4, and S6, for 72h, after which cells

were trypsinized, stained with trypan blue and counted using an automated cell counter (Invitrogen). Viable cell count values for the indicated samples were normalized to those obtained for vehicle (DMSO)-treated cells (control). Data are expressed as a percentage of inhibition relative to vehicle treated cells (control).

Xenograft Experiment

NT2197 mammary tumor cells ($5x10^4$) were injected into both sides of the fourth mammary fat pads of Nude mice (Charles River Laboratories). The mammary tumor growth (mm^3 ± SEM) was obtained by caliper measurements (n = 10 tumors/treatment group) and were calculated according to following formulae: $4/3\pi$ ($w^2 \times l$) as previously described, where l and w are diameter measurements of the length and width of the tumor, respectively (Ursini-Siegel et al., 2007). Once tumor volume reached 100∼200 mm^3, mice were given vehicle control (PBS;methylcellulose/Tween-80/DMSO), phenformin (50mg/kg) (Sigma-Aldrich P7045) via intraperitoneal injection, and/or lapatinib (50mg/kg) (lapatinib: LC Laboratories L-4804) via gavage every 24hr. All treatment conditions contained 12.5% DMSO and were resuspended in 0.5% methylcellulose-0.1% Tween-80 solution (Tween-80: Sigma-Aldrich P4780, methyl cellulose: 274429). On the day of necropsy mice were sacrificed 4h post-treatment, the mammary tumors were placed in 10% formalin to be fixed and later embedded in paraffin for immunohistochemistry. All animal experiments were performed in accordance with the guidelines of the McGill University animal ethics committee and the Canadian Council on Animal Care as approved by the facility animal care committee (protocol #5951).

Immunohistochemistry

Immunohistochemical staining of paraffin-embedded sections was performed as described previously (Ursini-Siegel et al., 2008), using the following antibodies: phospho-rpS6 (Ser240/244) (1:2000, CST 2215), phospho-AMPK (Thr172) (1:100, CST 2535), Ki67 (1:500, Abcam ab15580) and cleaved Caspase3 (1:250, CST 9661). Quantification of stained sections was performed using Aperio Imagescope software.

Western Blotting and Antibodies

Cells were lysed on ice in lysis buffer [50mM Tris/HCL pH 7.4, 5mM NaF, 5mM Na pyrophosphate, 1mM EDTA, 1mM EGTA, 250mM mannitol, 1% (v/v) triton x-100, 1mM DTT, 1X complete protease inhibitors (Roche), 1X PhosSTOP (Sigma-Aldrich)]. Protein concentrations in cell extracts were determined using Pierce BCA Protein Assay Kit (Thermo Fisher Scientific).

Proteins were resolved by SDS-PAGE, and then transferred to PVDF membranes (Bio-Rad). The following primary antibodies were used: anti-β-actin (Clone AC-15) #A1978, anti-HA #H6908, anti-PHGDH #HPA021241, from Sigma (Saint Louis, Missouri, USA); anti-4E-BP1(53H11) #9644, anti-p-4E-BP1 (Ser65) (174A9) #9456, anti-4E-BP2 #2845, anti-p-rpS6 (Ser240/244) #2215, anti-S6K #2708, anti p-S6K (Thr389) (#9234), anti ACC #3662, anti p-ACC (Ser79) #3661, anti ERK1/2 #9102, anti p-ERK1/2 (Thr202/Tyr204) #9101, anti eIF2α (L57A5) #2103, anti p-eIF2 α (Ser51) #9721, anti c-*myc* #9402, anti-Cyclin D3 (DCS22) #2936, anti-eIF4G1 #2858, anti-BCL-2 #2870, anti-TFAM #7495, anti-GAPDH (14C10) #2118, all from Cell Signaling Technologies (Danvers, MA, USA); anti-rpS6 (C-8) #sc-74459, anti-MCL-1(H-260) #sc-20679, anti-pyruvate carboxylase (PCB; H-300) #67021, from Santa Cruz Biotechnologies (Dallas, Texas, USA); anti-eIF4E #610269 from BD Biosciences (San Jose, CA, USA); anti-survivin #SURV11-S from Alpha Diagnostics (San Antonio, Texas, USA); anti-ASNS #NBP1-87444, anti-PSAT1 #NBP1-32920, anti-HIF-2α #NB100-122 from Novus Biologicals; HIF-1α # 10006421 from Cayman Chemical; anti-OGDH #ab87057, anti-GOT1 #ab189863, anti-survivin #ab175809, anti-TFAM #ab131607 from Abcam, and anti-puromycin 12D10 # MABE343 from Millipore. Antibodies were diluted in 5% (w/v) BSA or 5% (w/v) non-fat dry milk (depending on the manufacturer's instructions), in 1XTBS/0.5%Tween 20, at the following dilutions: 1:500 dilution for anti-HIF-2α and anti-survivin; 1:1000 dilution for anti-HA, anti-p-4E-BP1 (Ser65) (174A9), anti-4E-BP2, anti-S6K, anti p-S6K (Thr389), anti ACC, anti p-ACC (Ser79), anti ERK1/2, anti p-ERK1/2 (Thr202/Tyr204), anti eIF2α (L57A5), anti p-eIF2 α (Ser51), anti c-*myc*, anti-Cyclin D3 (DCS22), anti-eIF4G1, anti-BCL-2, anti-TFAM, anti-GAPDH (14C10), anti-MCL-1(H-260), anti-pyruvate carboxylase, anti-eIF4E, anti-survivin, anti-ASNS, anti-PSAT1, HIF-1α, anti-OGDH, anti-GOT1, anti-puromycin; and 1:5000 dilution for anti-β-actin, anti-PHGDH, anti-4E-BP1(53H11), anti-p-rpS6 (Ser240/244), and anti-rpS6. Membranes were incubated with antibodies overnight at 4°C. Horseradish peroxidase-conjugated anti-rabbit IgG and anti-mouse IgG antibodies were from Amersham Biosciences (Baie d'Urfé) and were used at 1:5,000 dilution in 5% (w/v) non-fat dry milk in 1XTBS/0.5%Tween 20 for 1 hour at room temperature. Signals were revealed by chemiluminescence (ECL, GE Healthcare) on HyBlot CL autoradiography film (Denville Scientific #E3018). Presented western blots are representative of at least 2-3 independent replicates. Where possible, the membranes were stripped and re-probed. In the cases when this resulted is extensive background, blots were run in parallel.

In Vitro Cap-Binding Affinity Assay

Experiments were carried out as previously described (Dowling et al., 2010). Briefly, cells were seeded in 150mm plates and treated as indicated in Figure 4 for 4h. Cells were washed with cold PBS, collected, and lysed in buffer containing 50mM MOPS/KOH (7.4), 100mM NaCl, 50 mM NaF, 2mM EDTA, 2mM EGTA, 1% NP40, 1% sodium deoxycholate, 7 mM β-mercaptoethanol, 1X complete protease inhibitors (Roche), and 1X PhosSTOP (Sigma-Aldrich). Lysates were incubated with m^7-GDP-agarose beads (Jena Bioscience) for 20 min at 4°C, washed 4 times with the washing buffer containing 50mM MOPS/KOH (7.4), 100mM NaCl, 50 mM NaF, 0.5mM EDTA, 0.5 mM EGTA, 7 mM β-mercaptoethanol, 0.5 mM PMSF, 1mM Na_3VO_4 and 0.1mM GTP, and bound proteins were eluted by boiling the beads in loading buffer. eIF4F complex formation was assessed by western blot of eluted proteins, using 4E-BP1, eIF4G1, eIF4E and β-actin antibodies as described in the "Western Blotting and Antibodies" section.

Proximity Ligation Assay (PLA)

Interactions between eIF4E and eIF4G1 (eIF4E–eIF4G) or eIF4E and 4E-BP1 (eIF4E–4E-BP1) were detected by *in situ* proximity ligation assay (PLA) on NMuMG-NT2197 cells according to the manufacturer's instructions (Duolink *In situ* red mouse/rabbit kit, Sigma). Briefly, 1.5x10^5 NT2197 control or 4E-BP1/2 DKO cells were seeded in six-well plates containing coverslips. The day after, cells were treated for 4 hours either with DMSO or combination of lapatinib (600nM) and phenformin (250 μM), washed with PBS and fixed in 3.7% formaldehyde for 15 min at room temperature. Cells were permeabilized for 10 min in PBS containing 0.2% Triton X-100, blocked for 45 min in PBS containing 10% FBS (blocking buffer) and incubated with primary antibodies (anti-eIF4E from Santa Cruz Biotechnologies SC-271480, 1:200; anti-eIF4G1 from Cell Signaling Technology #2498, 1:200 and anti-4E-BP1 from Cell Signaling Technology #9644, 1:500) overnight at 4°C. Secondary antibodies conjugated with PLA minus and PLA plus probes were incubated for 1 hour at 37°C. Ligation was performed for 30min at 37°C followed by amplification with polymerase for 2 hours at 37°C. Wheat germ agglutinin conjugated to Alexa fluor-488 (WGA, Life technologies), used to stain the plasma membrane, was incubated for 20 min at room temperature. Coverslips were mounted with O-link mounting medium containing DAPI (Sigma). Immunofluorescence microscopy images from single confocal sections were acquired at room temperature with a Wave FX spinning disc confocal microscope (Leica) using a 40X oil-immersion objective. All images were acquired using identical parameters. 10 images per condition were analyzed. Foci corresponding to eIF4E-eIF4G1 or eIF4E-4E-BP1 interactions and nuclei were detected and quantified using the Log-Dog Spot Counter in ImageJ (BAR. https://doi.org/10.5281/zenodo.28838). The number of PLA foci per cell were log2-transformed and represented as fold-change to DMSO. P values were calculated using one-way ANOVA (for eIF4E/4E-BP1) and Tukey test (for eIF4E–eIF4G1).

Flow Cytometry Analysis of Apoptotic Cells

NT2197 and RCC4 cells were plated in 6-well plates and grown for 24 h, after which they were treated as indicated in Figures S1, S2, S4, and S7, for 72h. Cells were trypsinized, counted and 100,000 cells were stained using either (Annexin V-FITC and PI) or (Annexin V-PE and 7-AAD) for 20min in the dark as per the manufacturer's instructions (FITC Annexin V Apoptosis Detection Kit, or PE Annexin V Apoptosis Detection Kit; BD Biosciences). Samples were analyzed with a LSR Fortessa cytometer (Becton Dickinson, Mountain View, CA). Fluorescence was detected by excitation at 488nm and acquisition on the 530/30-A channel for FITC-Annexin V, by excitation at 561nm and acquisition on the 610/20-A channel for PI, by excitation at 561nm and acquisition on the 582/15-A channel for PE-Annexin V and by excitation at 488nm and acquisition on the 695/40-A channel for 7-AAD. Cell populations were separated as follows: viable cells – Annexin V-/PI-, early apoptosis - Annexin V+/PI-, late apoptosis Annexin V+/PI+, dead Annexin V-/PI+; or viable cells – Annexin V-/7-AAD-, early apoptosis - Annexin V+/7-AAD-, late apoptosis Annexin V+/7-AAD+, dead Annexin V-/7-AAD+; and expressed as % of total single cells. Experiments were carried out 3 times independently (Figures S1K and S4I) or 2 times independently (Figures S2N and S7I), with 3 technical replicates in each experiment.

Flow Cytometry Analysis of Cytotoxicity

K562 cells were seeded in 6-well plates and grown for 24 h, after which they were treated, as indicated in Figure S2, with DMSO control, imatinib, phenformin or both for 72h. Cells were counted and 100,000 cells were stained using DAPI (4′,6-diamidino-2-phenylindole; 0.5 μg/mL) for 15min in the dark. Samples were analyzed with a LSR Fortessa cytometer (Becton Dickinson, Mountain View, CA). Fluorescence was detected by excitation at 405nm and acquisition on the 450/50-A channel. Cell populations with medium and high intensity DAPI stain were quantified. Experiments were carried out 3 times independently (n = 3), with 2 technical replicates in each experiment.

Measurement of ATP Levels

NT2197 cells were seeded at 5000/well in 96-well plates. 24h later, cells were treated as indicated in Figure S2J for 4h, with 3 technical replicates. ATP levels were assed using the Luminescent ATP Detection Assay Kit (Abcam), according to the manufacturer's instructions. The data have been normalized to the levels of control treated cells.

Polysome Profiles and RT-qPCR

Briefly, NT2197 CTR and 4E-BP1/2 CRISPR depleted cells were seeded in two 15cm Petri dish, harvested at 80% confluency and lysed in hypotonic lysis buffer (5mM Tris HCl pH7.5, 2.5mM $MgCl_2$, 1.5mM KCl, 100 μg/mL cycloheximide, 2mM DTT, 0.5% Triton, 0.5% Sodium Deoxycholate). Polysome-profiling was carried out as described (Gandin et al., 2014). Fractions were collected as described in Gandin et al. (2014) and RNA was extracted using Trizol (Thermo Fisher Scientific) according to manufacturer's instructions. RT-qPCR was performed as previously described (Miloslavski et al., 2014). RT and qPCR were performed by SuperScript III Reverse Transcriptase and Fast SYBR Green Mastermix (Invitrogen), respectively. Experiments were done at least in 2 independent experiments (n = 2) whereby every sample was analyzed in a technical triplicate. Analyses were carried out using relative standard curve method as described in http://www3.appliedbiosystems.com/cms/groups/mcb_support/documents/generaldocuments/cms_040980.pdf. Primers are listed in the Table S2 and the Key Resources Table. Polysome to 80S ratios were calculated by comparing the area under the 80S peak and the combined area under the polysome peaks.

Puromycilation Assay

NT2197 cells were maintained in puromycin free media for 48h. Then, cells were seeded in 100mm dishes for 24h, followed by 4h treatment as indicated in Figure S3I. During the last 15 min of treatment, puromycin (10 μg/mL) was added to the media. Cell lysates and western blot procedure were done as described in the "Western blotting and antibodies" section. Quantification of band intensities was done using ImageJ software (https://imagej.nih.gov/ij/index.html). Quantification was performed from 3 independent experiments and data was expressed as average ± SD of the reduction in puromycilation levels relative to DMSO control.

Glucose Consumption and Lactate Release Assays

NT2197 and A375 cells were seeded in 6-well plates and cultured in complete medium for 24h in order to obtain 30% density. Medium was replaced with 2ml of indicated treatment media, and cells were cultured for 22h. Treatment media was replaced with 0.7 to 1 mL of fresh treatment media for an additional 4h. Subsequently, supernatant samples were collected and cells were counted using an automated cell counter (Invitrogen). For K562, cells were seeded in 6-well plates and cultured in treatment media for 24h. Subsequently, supernatant samples were collected and cells were counted using an automated cell counter (Invitrogen). Measurement of glucose concentration in samples was done as previously described (Gravel et al., 2014). Total consumption was calculated by subtracting results from baseline glucose concentration, measured in samples from media incubated in identical conditions, without cells. Molar concentrations of glucose were multiplied by total media volume/well (0.7 to 1ml) and normalized per 10^6 cells; data were expressed as μM glucose/10^6cells/h, or normalized relative to DMSO control. Lactate release was quantified using a lactate assay kit (BioVision). Total secretion was calculated by subtracting results baseline lactate concentration, measured in samples from media incubated in identical conditions, without cells. Lactate production was normalized to cell count and data were expressed as percentage of control treated cells.

GC/MS and Stable Isotope Tracer Analyses of Cellular Samples

NT2197, A375 and RCC4 cells were cultured in 6-well plates to 80% confluency, after which indicated treatments was added to the media for 18-24 hours (as shown in figure legends). For stable isotope tracer analyses, prior to ^{13}C-glucose or ^{13}C-glutamine incubation, cells were maintained for 2h in a media of exact composition, but containing ^{12}C-glucose or ^{12}C-glutamine, for media equilibration purposes. The media was then exchanged for 10mM $^{13}C_6$-glucose (CLM-1396-PK; Sigma)-labeled media, 10mM 3-^{13}C-glucose (CLM-1393; Cambridge Isotope Laboratories)-labeled media, 4mM $^{13}C_5$-glutamine (CLM-1822-H-PK; Sigma)-labeled media for various periods from 3min to 4h30, as indicated. Cells were then rinsed three times with 4°C saline solution (9 g/L NaCl) and quenched with 600 μL 80% MEOH (< 20°C). Cells were removed from plates and transferred to prechilled tubes. MeOH quenching and harvest were repeated for a second time to ensure complete recovery. Membranes disruption was carried by sonication at 4°C (10 min, 30 s on, 30 s off, high setting, Diagenode Bioruptor). Extracts were cleared by centrifugation (14,000 rpm, 10min at 4°C) and supernatants were dried in a cold trap (Labconco) overnight at −4°C. Pellets were solubilized in 30 μL pyridine containing methoxyamine-HCl (10 mg/ mL, Sigma) by sonication and vortex, centrifuged and pellets were discarded. Samples were incubated for 30 min at 70°C (methoximation), and then were derivatized with MTBSTFA (70 μl, Sigma) at 70°C for 1 h. One μL was injected per sample for GC–MS analysis. GC–MS instrumentation and software were all from Agilent. GC–MS methods and mass isotopomer distribution analyses are as previously described (Morita et al., 2013). Data analyses were performed using the Chemstation software (Agilent, Santa Clara, USA). For steady state values, data were collected from 2-3 independent experiments, each consisting of 3 technical replicates. For isotope tracing experiments, data were collected from 2-3 independent experiments. Isotopomers content was followed at various time points (as indicated in the figures or figure legends) with single technical replicated.

GC/MS Analyses of Xenograft Tumor Metabolites

NT2197 mammary tumor cells ($5x10^4$) were injected into the right side of the fourth mammary fat pads of Nude mice (Charles River Laboratories). 16 days post-injection, mice were given vehicle control (PBS;methylcellulose/Tween-80/DMSO), phenformin (50mg/kg) (Sigma-Aldrich P7045) via intraperitoneal injection, and/or lapatinib (50mg/kg) (lapatinib: LC Laboratories L-4804) via gavage every 24hr, for 11 days. On day 11, 3h post-treatment, tumors were rapidly dissected, washed with saline, flash frozen in liquid nitrogen and kept at −80°C. All animal experiments were performed in accordance with the guidelines of the McGill University animal ethics committee and the Canadian Council on Animal Care as approved by the facility animal care committee (protocol #5518). Tumors were finely grounded in a mortar under liquid nitrogen, weighed and processed for GC/MS extraction (see section "Metabolite Extraction and GC/MS Analysis of Tumor Tissues").

In Vivo Infusions of ^{13}C- Labeled Glutamine

NT2197 mammary tumor cells ($5x10^4$) were injected into the right side of the fourth mammary fat pads of Nude mice (Charles River Laboratories). 26 days post-injection mice were infused via tail vein with $^{13}C_5$-glutamine (Cambridge Isotope Laboratories, Andover, MA) dissolved in saline. Briefly, mice were anesthetized with isoflurane and kept on a heating pad during the infusion process. A bolus of 0.3mg $^{13}C_5$glutamine/g mice was given followed by a continuous infusion at 0.15 μL/min/g mice weight for a duration of 120 min. This protocol yielded a final plasma glutamine enrichment of 34% on average. Tumors were rapidly dissected, washed with saline, flash frozen in liquid nitrogen and kept at −80°C. All animal experiments were performed in accordance with the guidelines of the McGill University animal ethics committee and the Canadian Council on Animal Care as approved by the facility animal care

committee (protocol #5518). Tumors were finely grounded in a mortar under liquid nitrogen, weighed and processed for GC/MS extraction (see section "Metabolite Extraction and GC/MS Analysis of Tumor Tissues").

Metabolite Extraction and GC/MS Analysis of Tumor Tissues

Approx. 15mg of ground tumor tissue was resuspended in ice-cold 80% methanol, followed by sonication and removal of debris by centrifugation at 4°C. Extracts were cleared by centrifugation (14,000 rpm, 4°C) and supernatants were dried in a cold trap (Labconco) overnight at −4°C. Pellets were solubilized in 30 μL pyridine containing methoxyamine-HCl (10 mg/ mL) by sonication and vortex, centrifuged and pellets were discarded. Samples were incubated for 30 min at 70°C (methoximation), and then were derivatized with MTBSTFA (70 μl, Sigma) at 70°C for 1 h. One μL was injected per sample for GC/MS analysis. Uniformly deuterated myristic acid (750 ng/sample) was added as an internal standard prior to extraction, and metabolite abundance was expressed relative to the internal standard and normalized to tissue weight. GC/MS instrumentation and software were from Agilent. GC/MS methods and mass isotopomer distribution analyses are as previously described (Gravel et al., 2016; Morita et al., 2013). Data analyses were performed using the Chemstation software (Agilent, Santa Clara, USA).

Quantification of Phenformin by LC-MS-MS

Plasma samples were spiked with internal standard [$^2H_4$]phenformin and deproteinized with a fourfold volume of 0.5% formic acid in acetonitrile. After dilution of the supernatant and an additional centrifugation step, phenformin was quantified by a validated assay based on LC-MS-MS. Tissue samples (20 – 30 mg) were homogenized in a total volume of 400 μl of 0.9% NaCl in a FastPrep 24 homogenizer (MP Biomedicals, Santa Ana, USA) for 20 s at speed 6.0 using lysing matrix D. The homogenate was centrifuged for 10 min at 15000 rpm. An aliquot of the supernatant was used for protein determination, in a further aliquot, phenformin was quantified as described for plasma samples.

LC-MS-MS Analysis

An Agilent 6460 triple quadrupole mass spectrometer (Agilent, Waldbronn, Germany) coupled to an Agilent 1200 HPLC system consisting of degasser G1379B, binary pump G1312B, well-plate sampler G1367D and column thermostat G1316B was used. Ionization mode was electrospray (ESI), polarity positive. Electrospray jetstream conditions were as follows: capillary voltage 3500 V, nozzle voltage 1000 V, drying gas flow 11 l/min nitrogen, drying gas temperature 300°C, nebulizer pressure 55 psi, sheath gas temperature 350°C, sheath gas flow 11 l/min. HPLC separation was achieved on a Synergi Polar-RP 80A column (150 × 2 mm I.D., 4 μm particle size, Phenomenex, Aschaffenburg, Germany) using (A) 0.1% formic acid in water and (B) 0.1% formic acid in acetonitrile as mobile phases at a flow rate of 0.4 mL/min. Gradient runs were programmed as follows: 10% B from 0 min to 2 min, linear increase to 50% B to 5 min, then re-equilibration. The mass spectrometer was operated in the multiple reaction monitoring (MRM) mode. MRM transitions, dwell time, fragmentor voltage and collision energy for analytes and internal standards are summarized below.

Analyte	MRM Transition (*m/z*)	Dwell Time (ms)	Fragmentor (V)	Collision Energy (V)
phenformin	206 > 60.1	100	92	13
[$^2H_4$]phenformin	210 > 60.1	100	92	13

Standardization and Validation

Calibration samples were prepared by adding varying amounts of metformin or phenformin to blank plasma and to untreated tissue homogenate, respectively. Concentration range was from 5 pmol to 5000 pmol per 25 μl of plasma or tissue homogenate for metformin and from 0.5 pmol to 500 pmol for phenformin. Calibration samples were worked up as described above, and analyzed together with the unknown samples. Calibration curves based on internal standard calibration were obtained by weighted (1/x) linear regression for the peak-area ratio of the analyte to the respective internal standard against the amount of the analyte. The concentration in unknown samples was obtained from the regression line. Assay accuracy and precision were determined by analyzing quality controls that were prepared like the calibration samples.

QUANTIFICATION AND STATISTICAL ANALYSIS

Statistical analysis was performed using 2-way ANOVA (Prism; Graphpad), unless otherwise specified. Technical replicates were averaged prior to statistical analysis; statistics were calculated by comparing 2-3 independent experiments each consisting of the averaged technical replicate result, and data was expressed as mean ± SD of data from independent experiments. Details on data quantification, presentation and statistical analysis specific for each experimental method are included in their respective STAR Methods sections, and in the figure legends.

DATA AND SOFTWARE AVAILABILITY

The original data have been deposited and are available at Mendeley Data: https://doi.org/10.17632/4k6knxb996.2.